

Impact of iron fertilisation on atmospheric CO₂ during the last glaciation

Himadri Saini^{1,2}, Katrin J. Meissner^{1,2}, Laurie Menviel^{1,3}, and Karin Kvale⁴

¹Climate Change Research Centre, University of New South Wales, Sydney, New South Wales, Australia

²The Australian Research Council Centre of Excellence for Climate Extremes, Sydney, New South Wales, Australia

³The Australian Centre for Excellence in Antarctic Science, University of Tasmania, Hobart, Tasmania 7001, Australia

⁴GNS Science, 1 Fairway Drive, Avalon 5010, P.O. Box 30368, Lower Hutt 5040, New Zealand

Correspondence: Himadri Saini (himadri.saini@student.unsw.edu.au)

Abstract. While several processes have been identified to explain the decrease in atmospheric CO₂ during glaciations, a better quantification of the contribution of each of these processes is needed. For example, enhanced aeolian iron input into the ocean during glacial times has been suggested to drive a 5 to 28 ppm atmospheric CO₂ decrease. Here, we constrain this contribution by performing a set of sensitivity experiments with different aeolian iron input patterns and iron solubility factors under boundary conditions corresponding to 70 thousand years before present (70 ka BP), a time period characterised by the first observed peak in glacial dust flux. We show that the decrease in CO₂ as a function of Southern Ocean iron input follows an exponential decay relationship. This exponential decay response arises due to the saturation of the biological pump efficiency and levels out at ~21 ppm in our simulations. We show that the changes in atmospheric CO₂ are more sensitive to the solubility of iron in the ocean, than the regional distribution of the iron fluxes. If surface water iron solubility is considered constant through time, we find a CO₂ draw-down of ~4 to ~8 ppm. However, there is evidence that iron solubility was higher during glacial times. A best estimate of solubility changing from 1% during interglacials to 3 to 5% under glacial conditions yields a ~9 to 11 ppm CO₂ decrease at 70 ka BP, while a plausible range of CO₂ draw-down between 4 to 16 ppm is obtained using the wider but possible range of 1 to 10%. This would account for ~12-50% of the reconstructed decrease in atmospheric CO₂ (~32 ppm) between 71 and 64 ka BP. We further find that in our simulations the decrease in atmospheric CO₂ concentration is solely driven by iron fluxes south of the Antarctic polar front, while iron fertilization elsewhere plays a negligible role.

1 Introduction

CO₂ draw-down during the last glacial period occurred in multiple steps before reaching a minimum level of ~190 ppm at the Last Glacial Maximum (LGM, 21,000 years ago) (EPICA Community Members et al., 2004; Ahn and Brook, 2008; Lüthi et al., 2008; Bereiter et al., 2012, 2015). One of the last major drops in atmospheric CO₂ concentration occurred at the beginning of Marine Isotope Stage (MIS) 4 (71-59 thousand years ago, ka BP hereafter) when CO₂ decreased from 233±8 ppm to 201±4 between 71 ka and 64 ka (Figure 1b). This period also coincided with the minimum summer insolation at high northern latitudes (~70 ka BP, Berger (1978)), which led to the most pronounced episode of ice sheet growth in the Northern Hemisphere (NH) over the glaciation (Bassinot et al., 1994; Petit et al., 1999; Grant et al., 2012). Even though NH ice sheet extent

and volume during MIS4 and MIS3 are not well constrained, numerical modelling experiments and observational records have
25 shown that the extent of the Cordilleran and Scandinavian ice sheets was larger during MIS4 than during the LGM, whereas
the Laurentide and Greenland ice sheets were smaller (Lambeck et al., 2010; Kleman et al., 2013; Batchelor et al., 2019). As
a result of the glaciation occurring during the early part of MIS4, it is suggested that the global sea level dropped to about
80m below present day sea level (Waelbroeck et al., 2002; Grant et al., 2012; Batchelor et al., 2019; De Deckker et al., 2019).
Global sea surface temperatures (SSTs) also show a rapid decline by $\sim 1^\circ\text{C}$ in the early MIS4 transition and an overall $\sim 1.5^\circ$
30 drop across MIS4, before rising again to pre-MIS4 levels around 59 ka BP (Kohfeld and Chase, 2017).

Several mechanisms have been put forward to explain the draw-down of atmospheric CO_2 during glaciations, including the
 ~ 32 ppm drop in CO_2 during the MIS4 transition. These mechanisms include higher solubility of CO_2 in colder ocean waters
(Heinze et al., 1991; Kucera et al., 2005; Williams and Follows, 2011; Khatiwala et al., 2019); higher carbon sequestration
35 associated with a weaker Atlantic Meridional Overturning Circulation (AMOC) and thus lower ventilation rates during glacial
periods (Sigman and Boyle, 2000; Toggweiler, 2008; Sigman et al., 2010; Watson et al., 2015; Jaccard et al., 2016; Yu et al.,
2016; Menviel et al., 2017; Kohfeld and Chase, 2017); and the expansion of sea ice cover leading to more stratified Southern
Ocean (SO) waters and smaller air-sea gas exchange (Francois et al., 1997; Stephens and Keeling, 2000; Ferrari et al., 2014).
However, it has been argued that sea ice expansion does not correlate well with the timing of CO_2 draw-down at 70 ka (Kohfeld
40 and Chase, 2017), and that the major drivers during this transition might in fact be due to a shallower AMOC (Piotrowski et al.,
2005; Thornalley et al., 2013; Yu et al., 2016), or a more efficient biological pump due to enhanced iron input to the ocean
(Brovkin et al., 2012; Menviel et al., 2012; Anderson et al., 2014; Lamy et al., 2014; Martínez-García et al., 2014). Interestingly,
high resolution $\delta^{13}\text{CO}_2$ records from Antarctic ice cores (Menking et al., 2022) display a 0.5 permil decrease centred at 70.5
ka, followed by a 0.7 permil increase (Figure 1g), indicating a complex set of processes impacting atmospheric CO_2 at the
45 MIS5-4 transition. While surface ocean cooling could explain the concurrent CO_2 and $\delta^{13}\text{CO}_2$ decrease, the $\delta^{13}\text{CO}_2$ increase
in the second part of the transition would be consistent with a greater efficiency of the biological pump and increased storage
of respired carbon in the deep ocean (Menviel et al., 2015; Eggleston et al., 2016; Menking et al., 2022).

The efficiency of the biological pump is partly dependent on the relative abundance of different marine phytoplankton
communities, which further depends on the availability of both macro and micro nutrients (Kvale et al., 2015a; Saini et al.,
50 2021). Martin (1990) suggested that the micro nutrient iron plays a crucial role as a limiting nutrient in phytoplankton growth,
and thus put forward the hypothesis that iron fertilisation, resulting from an increase in atmospheric dust during glacial times,
might have increased marine net primary production (NPP) in the Southern Ocean, leading to a decrease in atmospheric CO_2
concentration. Antarctic ice core records indeed show peaks in dust fluxes that coincide with lower Antarctic temperatures and
lower CO_2 levels (Figure 1) during MIS4 and MIS2 (27-19 ka) (Wolff et al., 2006, 2010; Lambert et al., 2008, 2012; Martínez-
55 García et al., 2011, 2014; Lamy et al., 2014). These peaks in dust flux are concurrent with increased export production (EP) in
the subantarctic zone (SAZ) of the Southern Ocean during the LGM (Kohfeld et al., 2005, 2013; Martínez-García et al., 2014),
as well as during MIS4 (Lamy et al., 2014; Martínez-García et al., 2014; Thöle et al., 2019; Amsler et al., 2022). On the other

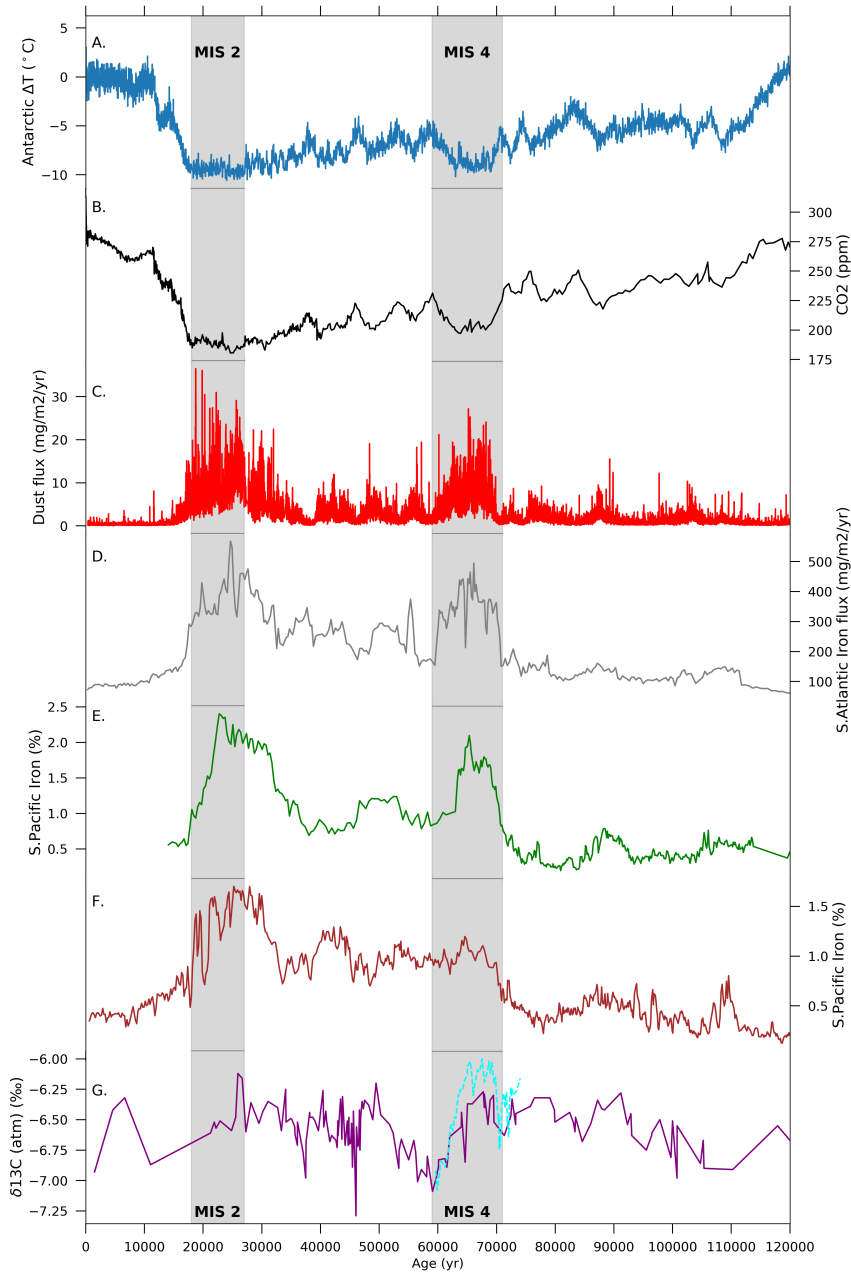


Figure 1. Time series of (a) Antarctic temperature anomalies from present day ($^{\circ}\text{C}$) (Jouzel et al., 2007), (b) atmospheric CO_2 concentration (ppm) (Bereiter et al., 2015), and (c) dust flux ($\text{mg}/\text{m}^2/\text{yr}$) (Lambert et al., 2012) as recorded in EPICA DOME C ice core; (d) iron dust accumulation rates ($\text{mg}/\text{m}^2/\text{yr}$) from ODP Site 177-1090 (Atlantic) (Martínez-García et al., 2011); iron (%) records in the South Pacific from Lamy et al. (2014) at sites (e) PS75-076 and (f) PS75-059; (g) atmospheric $\delta^{13}\text{C}$ (‰) as recorded in a composite of Antarctic ice cores (purple line, Eggleston et al. (2016)) and high resolution records from Taylor Glacier ice cores (dashed cyan line, Menking et al. (2022)). Shaded areas represent marine isotope stages 2 (MIS2: 27-19 ka BP) and 4 (MIS4: 71-59 ka BP).

hand, palaeoceanographic data from the Antarctic zone (AZ) suggest a decrease in EP at the LGM and MIS4 (Kohfeld et al., 2005, 2013; Anderson et al., 2009; Jaccard et al., 2013; Studer et al., 2015; Thöle et al., 2019; Amsler et al., 2022).

60 Numerous modelling studies have explored the changes in Southern Ocean biogeochemistry due to enhanced aeolian iron input either under pre-industrial (PI) (Aumont and Bopp, 2006; Tagliabue et al., 2009a, 2014) or LGM conditions (Aumont et al., 2003; Bopp et al., 2003; Oka et al., 2011; Lambert et al., 2015; Muglia et al., 2017; Khatiwala et al., 2019; Yamamoto et al., 2019; Lambert et al., 2021; Saini et al., 2021), but not under MIS4 conditions. An exception is Menviel et al. (2012) who simulated a ~ 12 ppm CO₂ drop as a result of enhanced aeolian iron fluxes into the Southern Ocean at 70 ka in a transient
65 simulation of the last glacial cycle.

In this study, we constrain the impact of enhanced aeolian iron input on atmospheric CO₂ concentration during the MIS4 transition. We perform a set of sensitivity experiments with different aeolian iron flux masks and different iron solubilities under 70 ka boundary conditions, using a model of intermediate complexity, which includes an ocean general circulation model (OGCM) coupled to a recently developed complex ecosystem model (Kvale et al., 2021; Saini et al., 2021). The ecosystem
70 model used here includes calcifying and silicifying plankton and an iron cycle, which makes it well-suited for studying CO₂ uptake in the Southern Ocean.

2 Methods

2.1 Model description

This study uses the 2.9 version of the University of Victoria Earth System Climate Model (UVic ESCM), which consists of a
75 sea ice model (Semtner Jr, 1976; Hibler, 1979; Hunke and Dukowicz, 1997) coupled to the ocean general circulation model MOM2 (Pacanowski, 1995), with 19 ocean depth layers and a spatial resolution of 3.6° by 1.8°. It also includes a dynamic vegetation model (Meissner et al., 2003), a land surface scheme (Meissner et al., 2003), a 2-D atmospheric energy moisture balance model integrated vertically (Fanning and Weaver, 1996) and a sediment model (Archer and Maier-Reimer, 1994; Meissner et al., 2012). The model is forced with seasonally varying wind stress and wind fields (Kalnay et al., 1996) and
80 seasonal variations in solar insolation at the top of the atmosphere. Full physical and structural descriptions of the model can be found in Weaver et al. (2001), Meissner et al. (2003), Eby et al. (2009), and Mengis et al. (2020).

The marine carbon cycle is represented by the newly developed Kiel Marine Biogeochemistry Model, version 3 (KMBM3) (Kvale et al., 2021) which is based on the Nutrient Phytoplankton Detritus Zooplankton model of Schmittner et al. (2005) and Keller et al. (2012). There are four different classes for phytoplankton in this ecosystem model. Three of which include
85 specifically characterized plankton such as diazotrophs that can fix nitrogen, coccolithophores that produce CaCO₃ shells, and diatoms that produce opal. The fourth class is for the rest of the types of plankton, that are mostly located in the low latitude regions. The model also includes prognostic CaCO₃ and silica tracers (Kvale et al., 2015b, a, 2021), dissolved nitrate, phosphate, iron, and silica as nutrients. The model also incorporates an iron cycle (Nickelsen et al., 2015), including hydrothermal sources. The ecosystem model is described in detail in Kvale et al. (2021).

Table 1. Aeolian iron fluxes for each experiment.

Experiment	Total iron flux into the ocean (Gmol yr^{-1})	Iron flux into the Southern Ocean south of 47°S (Gmol yr^{-1})
PI-control (pife1%)	3.47	0.092
70ka-control (pife1%)	3.47	0.092
lambfe1%	9.072	0.461
lambfe3%	27.44	1.383
lambfe5%	45.73	2.305
lambfe7%	64.02	3.227
lambfe10%	91.46	4.610
lambfe20%	182.9	9.221
glacfe1%	6.532	0.4425
glacfe3%	19.6	1.328
glacfe10%	65.32	4.425
glacfe20%	139.1	8.850
lambfe10%-30S	18.51	4.610
lambfe10%-40S	13.94	4.610
lambfe10%-50S	6.05	2.66
lambfe10%-60S	3.9	0.5
lambfe50%-47S	27.09	23.05
pife3%	10.41	0.27
pife5%	17.35	0.46
pife7%	24.29	0.64
pife10%	34.7	0.92
pife20%	69.4	1.84

90 2.2 Experimental design

A pre-industrial control simulation (PI-control) is integrated under PI boundary conditions, including an atmospheric CO₂ concentration of 283.86 ppm, and PI iron (pife) and silica (pisi) fluxes. The PI aeolian dust fluxes are based on the PI-BASE dust flux simulation of Mahowald et al. (2006). To obtain iron and silica fluxes, we multiply the dust flux with the percentage distribution of iron and silica in dust (Zhang et al., 2015), respectively. The solubility factor for iron in the PI-control simulation is set to 1%.

All the other experiments are run under 70 ka boundary conditions, including orbital parameters corresponding to the year 70 ka BP according to Berger (1978), and a continental ice sheet topography generated by an offline ice-sheet simulation performed with IcIES (Ice sheet model for Integrated Earth system Studies, Abe-Ouchi et al. (2013)). The global mean ocean alkalinity was adjusted on the basis of sea level differences. For the control simulation (70ka-control), the model is run into

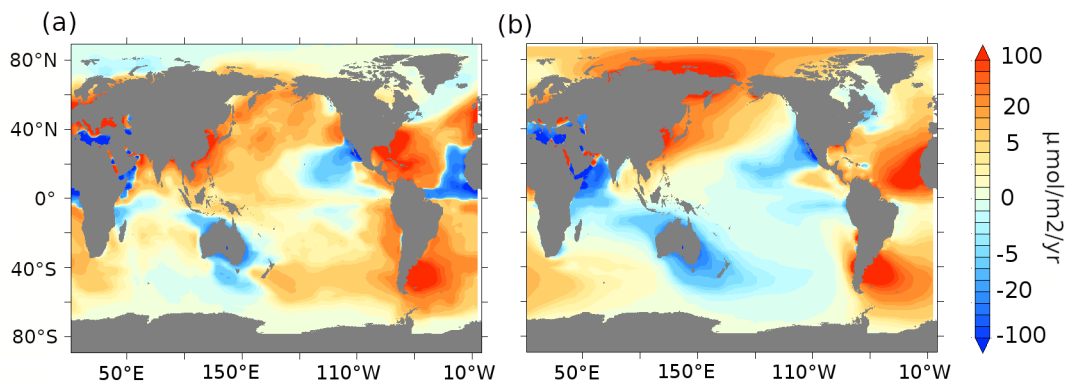


Figure 2. Aeolian iron dust flux ($\mu\text{mol m}^{-2} \text{yr}^{-1}$) anomalies for (a) lambfe1% minus pife1% and (b) glacfe1% minus pife1%.

100 equilibrium with an atmospheric CO_2 concentration of 222.5 ppm (Bereiter et al., 2015), after which the simulation is integrated for an additional 200 years with prognostic atmospheric CO_2 . 70ka-control is forced with pife (with 1% iron solubility) and pisi fluxes.

From this control simulation, we branch off a suite of sensitivity experiments with prognostic atmospheric CO_2 , using two different glacial iron dust flux estimates. The first iron flux, lambfe, is obtained from the LGM dust estimates of Lambert et al. (2015). This dust flux estimate is calculated by performing a global 2-d interpolation on unevenly distributed LGM dust flux records, most of which are collated in the DIRTMAP (Dust Indicators and Records of Terrestrial and Marine Paleoenvironments) database (Kohfeld and Harrison, 2001; Maher et al., 2010). Their interpolation method assumes that the aerosol concentration in the air decreases exponentially from the source distance. The second iron flux, glacfe, is derived from a dust flux obtained with a model (LGMglac.a, Ohgaito et al. (2018)). This model includes glaciogenic dust sources in addition to the usual desert dust sources and assumes dry and unvegetated regions as dust sources. It then calculates global dust transport and deposition. Both glacfe and lambfe are then obtained in this study by mapping the iron percentage on dust (Zhang et al., 2015) as mentioned above. The aeolian iron fluxes based on glacfe and lambfe dust patterns compared to the PI iron flux (pife), and assuming a 1% solubility, are shown in Figure 2, while the full dust deposition maps for PI and the two LGM reconstructions are available in the supplementary material of Saini et al. (2021).

115 The iron delivered to the ocean surface via aeolian dust deposition needs to be dissolved before it can become available to phytoplankton. The solubility factor of iron is therefore an important parameter that will impact the magnitude of iron fertilization. Iron solubility varies depending on both provenance and speciation. For example, Baker et al. (2006) find that solubilities in samples of Saharan dust (median of 1.7%) are significantly lower than solubilities in aerosols from other source regions feeding into the Atlantic ocean (median of 5.2%). Schroth et al. (2009) find a significant difference in iron solubility between arid soils (1%), glacial flour (2-3%) and, of lesser importance to our study, oil combustion products (77-81%). In the present day Southern Ocean, observations of iron solubilities vary between 0.2 and 48% (Ito et al., 2019), with the higher values being hypothesized to be caused by pyrogenic iron. The majority of the observational data in the present day Southern Ocean

lies between 1 and 12% (Ito et al., 2019). Quantifying iron solubilities during past climates is even more challenging. Conway et al. (2015) estimate iron solubility at the Last Glacial Maximum (LGM) based on dust particles in the EPICA Dome C and Berkner Island ice cores. They find that iron solubility was very variable during the LGM interval at Dome C (1-42%), with a mean of 10% and a median of 6%. On the other hand, iron solubility at Berkner Island was 1-5% at the LGM, and in average ~3% between 23 and 50 ka. The lower iron solubility at Berkner Island is thought to be due to the aerosol composition. Due to its proximity to South America, the solubility found at Berkner island might better represent large-scale aeolian dust deposited in the Southern Ocean. Iron is more bioavailable in dust that originates from physically weathered than from chemically weathered bedrock (Shoenfelt et al., 2017). The analysis of subantarctic marine sediment cores further suggests that aeolian iron was 15 to 20 times more bioavailable during glacial periods than during the current interglacial (Shoenfelt et al., 2018).

In this study, we test a global mean solubility range of 1% to 20% (Table 1). Based on the studies mentioned above, we define the plausible range of average iron solubility to be 1 to 10%, with an increased likelihood at 3-5% during colder climate episodes. During warmer climates, such as PI or at the MIS4 onset, we define the most likely solubility factor as 1%.

However, due to the uncertainties associated with present-day iron solubilities, we perform additional sensitivity experiments under 70 ka BP boundary conditions using the PI iron dust mask with iron solubility varying between 3% and 20%. This approach allows us to estimate the minimum change in CO₂ due to glacial dust fluxes, assuming no change in solubility over time. The corresponding CO₂ changes can be calculated by taking the difference between CO₂ changes achieved with the full experiments (i.e., changing masks and solubilities) and the CO₂ changes achieved by only changing solubility. This approach was validated by performing two additional 70ka equilibrium experiments with the pife mask and an iron solubility of 3% and 10% from which we branched off simulations with the lambfe mask and constant solubility (not shown). The resulting CO₂ drawdown in these experiments was the same than if calculated as the difference between the full experiments and solubility-only experiments. The integrated aeolian iron input for all experiments is listed in Table 1.

We perform five additional sensitivity experiments (Figure A1) to better quantify the contribution of the Southern Ocean to the total CO₂ draw-down. In these experiments, the aeolian iron flux in the Southern Ocean follows the lambfe mask while the PI aeolian iron fluxes are applied outside of the Southern Ocean. In four of these experiments (lambfe10%-30S, lambfe10%-40S, lambfe10%-50S, lambfe10%-60S), the lambfe mask with 10% solubility (Figure A2) is applied south of 30°S, 40°S, 50°S and 60°S, respectively. In the fifth sensitivity experiment (lambfe50%-47S), the aeolian iron input south of 47°S follows the lambfe mask with a solubility factor of 50% (Figure A1f), which is equivalent to 23.05 Gmol_{yr}⁻¹ iron input in the Southern Ocean south of 47°S and provides an upper limit on the potential CO₂ draw-down.

2.3 Carbon decomposition

To better understand the changes in ocean carbon, we decompose the simulated dissolved inorganic carbon (DIC) into its three major components: respired organic carbon (C_{reg}), DIC generated by dissolution of calcium carbonate (C_{CaCO_3}) and preformed carbon (C_{pref}) as described below.

C_{reg} is calculated based on the remineralized phosphate in the ocean (P_{reg}) and the carbon to phosphate stoichiometric ratio ($R_{C/P}=106$):

$$\Delta C_{reg} = \Delta P_{reg} \times R_{C/P} \quad (1)$$

P_{reg} is determined based on Apparent Oxygen Utilisation (AOU) and the phosphate to oxygen stoichiometric ratio ($R_{P/O_2}=1/160$), $\Delta P_{reg} = \Delta AOU \times R_{P/O_2}$, where AOU is calculated as the difference between the saturated oxygen concentration (O_{2sat}) and the dissolved oxygen concentration in the ocean (O_2); $AOU = O_{2sat} - O_2$.

C_{CaCO_3} is calculated as:

$$\Delta C_{CaCO_3} = 0.5(\Delta ALK + R_{N/P} \times \Delta P_{tot}) \quad (2)$$

where $R_{N/P}=16$. And finally, C_{pref} is calculated as the remainder:

$$\Delta C_{pref} = \Delta DIC - \Delta C_{reg} - \Delta C_{CaCO_3} \quad (3)$$

To further assess the efficiency of the biological pump, we calculate global P^* (Ito and Follows, 2005), defined as:

$$P^* = P_{reg}/P_{total} \quad (4)$$

where P_{total} is the total phosphate content in the ocean.

3 Results

3.1 Simulated ocean conditions at 70 ka BP

In this section, we describe the simulated physical and biological conditions at 70 ka BP, at the onset of MIS4 (Figure 3). In our 70ka-control simulation, the globally averaged ocean temperature is $\sim 2.8^\circ\text{C}$, about 0.6°C lower than in PI-control, but 0.9°C higher than in a LGM simulation integrated with the same model (Saini et al., 2021). The globally averaged annual mean SST is 17.1°C , 0.8 degrees lower than in the PI-control and 1.1 degrees higher than in the LGM simulation. The strongest ocean surface cooling (-1.45°C) at 70 ka BP with respect to our PI-control is simulated north of 40°N in the Atlantic and Pacific oceans, while the annual mean SSTs in the SAZ and AZ are $\sim 0.8^\circ\text{C}$ and 0.4°C lower than in the PI-control, respectively (Figure 3a). At 70 ka BP, the annual mean Southern Ocean sea ice edge is situated at 55°S in the South Atlantic and the South Indian Ocean, ~ 1 degree further north than in the PI-control simulation, while the change is insignificant in the South Pacific sector (sea ice edge at $\sim 62^\circ\text{S}$). The simulated AMOC strength in the 70ka-control experiment is ~ 14 Sv, compared to ~ 17 Sv in the PI-control, without significant changes in its depth (Figure A3). Furthermore, there are no significant changes in simulated Antarctic Bottom Water (AABW) formation (Figure 3c, d).

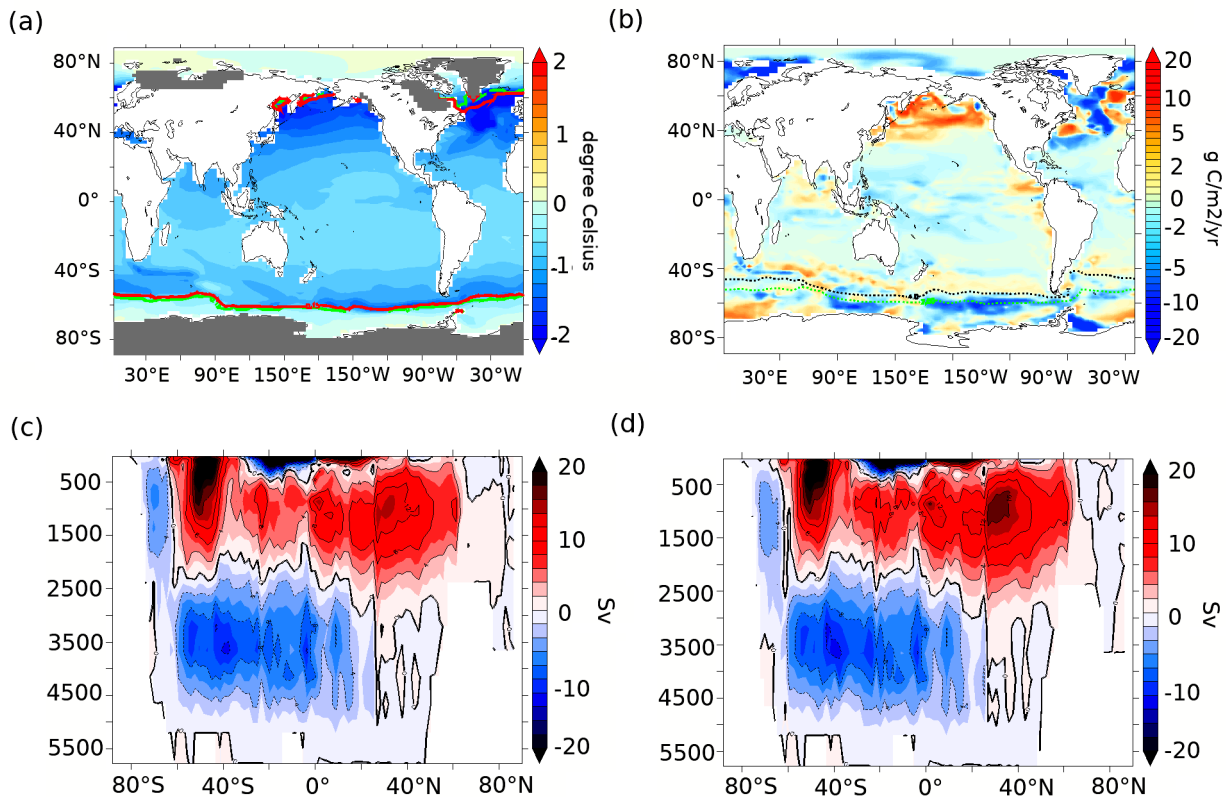


Figure 3. (a) Annual mean SST anomalies ($^{\circ}\text{C}$, shading) at 70 ka BP compared to PI and 15% annual mean sea-ice concentration at PI (green line) and 70 ka BP (red line). The grey shading on land shows the extent of continental ice sheets at 70 ka BP (Abe-Ouchi et al., 2013); (b) Export production anomalies between 70 ka BP and PI at 177.5m depth ($\text{g C m}^{-2} \text{ yr}^{-1}$). Overlaid dashed contours represents modern subantarctic front (SAF) in black and Antarctic polar front (APF) in green based on Sokolov and Rintoul (2009); Global overturning streamfunction (Sv) at (c) 70 ka BP and (d) PI.

The colder conditions, more extensive sea-ice cover, and changes in the deep ocean convection impact marine productivity (Saini et al., 2021). Globally, NPP decreases by $\sim 9.7\%$, while EP decreases by $\sim 3\%$ in our 70ka-control simulation compared to PI-control (both integrated with the pife mask and 1% iron solubility, Table A1). The simulated 18% EP increase at 70 ka in the North Pacific (Figure 3b) can be attributed to a greater diatom and coccolithophore abundance in that region (Figure A4a, 185 b) resulting from higher nutrient availability. This EP increase in the North Pacific is however inconsistent with the biogenic Ba (Jaccard et al., 2005) and $\delta^{15}\text{N}$ (Gebhardt et al., 2008) records from the sub-arctic North Pacific which suggest a decrease in EP at MIS4 onset. The North Atlantic shows a complex pattern of anomalies due to changes in the strength and location of deep ocean convection, which result in an overall decrease in NPP and EP by 16% and 9%, respectively.

Within the AZ (south of the APF), diatoms decrease by 14% in the Pacific, while they increase by 3% in the Atlantic and 190 Indian sectors (Figure A4a). The decrease in diatoms in the Pacific sector of the AZ leads to a competitive growth advantage

Table 2. ΔCO_2 simulated by changing the iron mask from PI to glacial (lambfe and glacfe) at 70 ka BP but keeping the solubility constant.

Solubility	ΔCO_2 (lambfe-pife)	ΔCO_2 (glacfe- pife)
1%	-3.8	-5.1
3%	-6.4	-8.2
5%	-6.9	-
7%	-7.5	-
10%	-7.3	-8.3
20%	-6.7	-6.9

for coccolithophores, which increase by 6.5% south of the polar front, thus leading to a poleward shift of coccolithophores in the Pacific sector (Figure A4b). On the other hand, coccolithophores decrease in the Atlantic and Indian sectors of the AZ by 15% and 8%, respectively. Diatoms increase by 22% in the SAZ (north of the SAF) while there are no significant changes in coccolithophores abundance. As a result of the changes in these two plankton species, EP increases by 1.3% in the SAZ and decreases by 14% in the AZ (Figure 3b). The total Southern Ocean (south of 30°S) EP and NPP decrease by 2% and 7.5%, respectively at 70 ka.

3.2 Impact of changes in iron dust flux on atmospheric CO_2

Changing the iron flux masks from PI to glacial at 70 ka BP leads to a 3.8 to 8.3 ppm drop in atmospheric CO_2 concentration if we assume that the mean iron solubility remains unchanged (Table 2). Interestingly, for solubilities of 3% and higher, the drawdown is nearly constant, regardless of the glacial dust flux mask and regardless of the solubility (7.3 ± 1 ppm).

However, the solubility of iron was likely higher during cold than warm periods (see section 2.2). We will therefore discuss experiments that switch from a PI iron mask with 1% solubility to glacial iron masks with higher solubilities from hereon. These experiments show a ~ 9 to 19 ppm drop in atmospheric CO_2 concentration (Figure 4a and b, Table 3). These changes in atmospheric CO_2 impact the physical conditions of the ocean only slightly in our model. As such, the global overturning circulation, mean SST and sea-ice extent are similar in most of the sensitivity experiments described below.

As the global and Southern Ocean iron input increase, the atmospheric CO_2 concentration decreases, but not linearly, as the efficiency of the iron fertilisation weakens with the increasing iron availability (Figure 4a,b). The patterns of aeolian iron deposition in the Southern Ocean are different for the two masks used here. Both reconstructions show an increase in the South Atlantic sector compared to PI fluxes, but they differ over the Pacific and Indian sectors, including large regions where dust deposition decreases compared to PI (Figure 2). It is therefore interesting that our experiments with similar total iron input into the Southern Ocean but different regional patterns (e.g. glacfe20% and lambfe20%, Figure 4b, pink star and black circle) display similar efficiency in drawing down CO_2 regardless of the dust mask used. The glacfe mask is however slightly more efficient in drawing down atmospheric CO_2 . The iron flux into the South Atlantic sector is higher in the glacfe mask compared to the lambfe mask, increasing iron concentrations near one of our major convection sites in the Weddell Sea. Bottom water

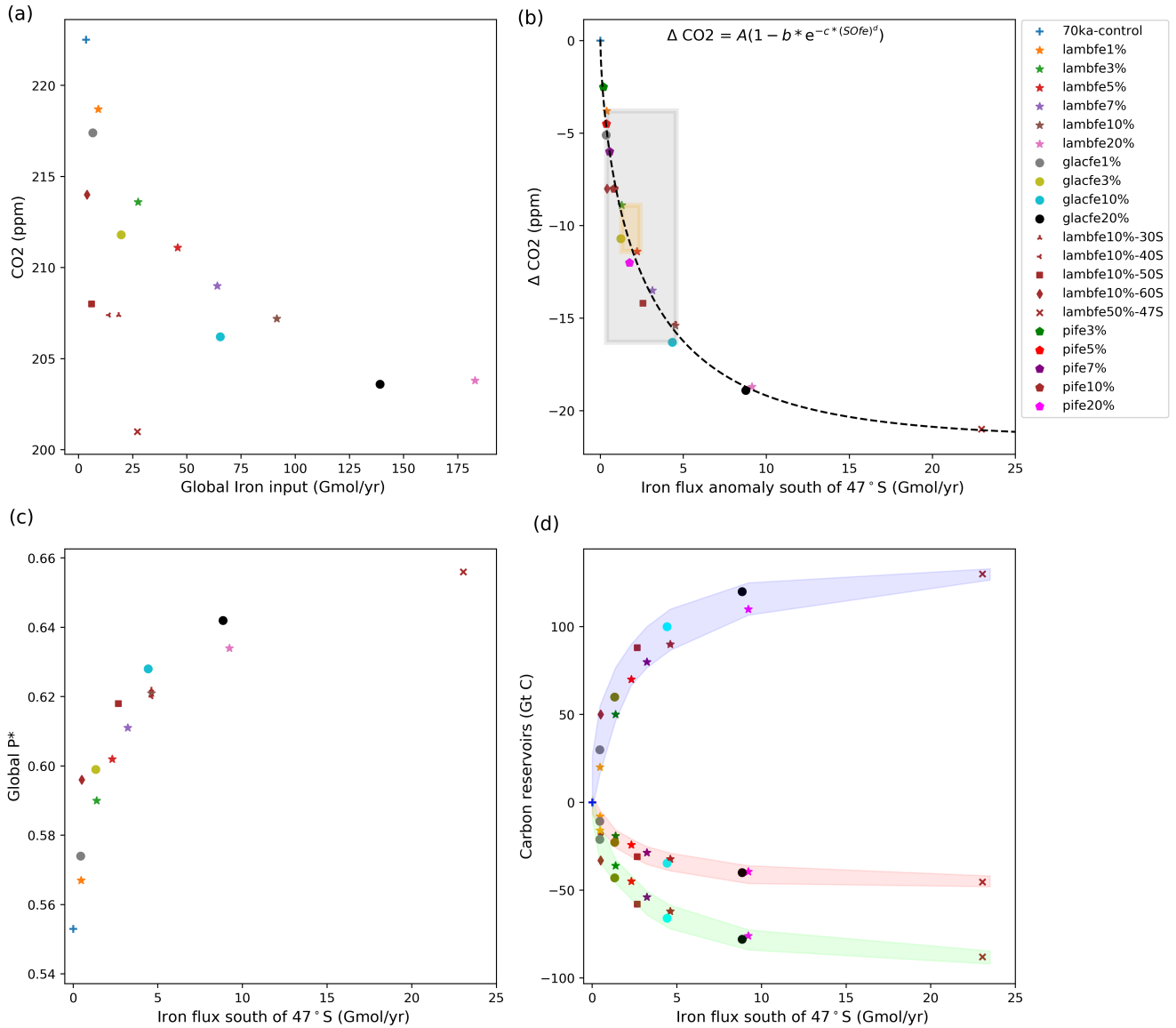


Figure 4. (a) Equilibrated atmospheric CO₂ concentration (ppm) as a function of the globally integrated aeolian iron flux into the ocean (Gmol/yr⁻¹). (b) Atmospheric ΔCO₂ concentration (ppm) as a function of changes in aeolian iron flux into the Southern Ocean south of 47°S. The grey shading represents the range of likely glacial iron solubilities (1-10%) and the associated change in CO₂ concentration (-4 to -16 ppm), while the orange shading represents our best estimate of change in CO₂ (-9 to -11 ppm) for a solubility of 1% during warm periods and 3-5% during colder periods. Note that lambfe10%, lambfe10%-30S and lambfe10%-40S are overlapping. The black curve represents the best fit and suggests a maximum CO₂ draw-down of ~21 ppm due to Southern Ocean iron fertilisation. (c) Global P* as a function of aeolian iron flux into the Southern Ocean south of 47°S and (d) Globally integrated carbon reservoirs (Gt C) as a function of aeolian iron flux into the Southern Ocean south of 47°S. The shadings represent ocean carbon (blue), atmospheric carbon (red) and terrestrial carbon (green).

Table 3. ΔCO_2 for the sensitivity experiments compared to 70 ka-control, globally averaged P^* values, as well as NPP and EP values integrated over different regions of the Southern Ocean. Percentage changes from 70ka-control experiment are provided in brackets

Experiment	ΔCO_2 (ppm)	Global P^*	SO NPP (30°S:90°S, Pg Cyr^{-1})	SO NPP north of 47°S (Pg Cyr^{-1})	SO NPP south of 47°S (Pg Cyr^{-1})	SO EP (30°S:90°S, Pg Cyr^{-1})	SO EP north of 47°S (Pg C yr^{-1})	SO EP south of 47°S (Pg C yr^{-1})
PI-control (pife1%)	-	0.515	14.63	7.62	7	3.84	1.58	2.267
70ka-control (pife1%)	0	0.553	13.52	5.38	8.15	3.76	1.13	2.63
lambfe1%	-3.8	0.566	13.58 (+0.4%)	4.55 (-15%)	9.04 (+11%)	3.93 (+4.5%)	0.99 (-12%)	2.93 (+11.6%)
lambfe3%	-8.9	0.590	13.43 (-0.6%)	3.77 (-30%)	9.68 (+18.7%)	4.08 (+8.6%)	0.84 (-25%)	3.23 (+23%)
lambfe5%	-11.4	0.602	13.36 (-1.1%)	3.47 (-35%)	9.89 (+21%)	4.14 (+10.3%)	0.79 (-30%)	3.36 (+30%)
lambfe7%	-13.5	0.611	13.31 (-1.5%)	3.31 (-38%)	10.02 (+23%)	4.19 (+11.4%)	0.75 (-33%)	3.44 (+30.7%)
lambfe10%	-15.3	0.621	13.27 (-1.8%)	3.16 (-41%)	10.12 (+24%)	4.22 (+12.4%)	0.72 (-36%)	3.5 (+33%)
lambfe20%	-18.7	0.634	13.35 (-1.2%)	3.01 (-44%)	10.35 (+27%)	4.33 (+15%)	0.68 (-39%)	3.64 (+38.5%)
glacfe1%	-5.1	0.574	13.39 (-0.9%)	4.43 (-17.6%)	8.97 (+10%)	3.92 (+4.3%)	0.97 (-13.7%)	2.94 (+12%)
glacfe3%	-10.7	0.599	13.21 (-2.2%)	3.60 (-33%)	9.62 (+18%)	4.07 (+8.2%)	0.81 (-28%)	3.25 (+23.8%)
glacfe10%	-16.3	0.628	13.14 (-2.8%)	3.12 (-42%)	10.03 (+23%)	4.20 (+11.7%)	0.71 (-37%)	3.5 (+32.8%)
glacfe20%	-18.9	0.642	13.09 (-3.1%)	2.98 (-45%)	10.12 (+24%)	4.25 (+13%)	0.68 (-40%)	3.57 (+36%)

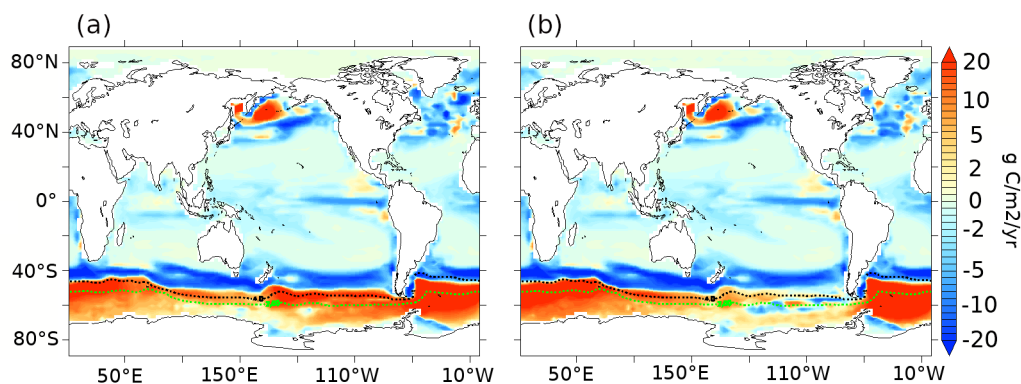


Figure 5. Export production anomalies ($\text{gC m}^{-2} \text{yr}^{-1}$) at 177.5m depth for (a) lambfe3% and (b) glacfe3% compared to 70ka-control (pife1%). Overlaid dashed contours represents modern SAF in black and APF in green based on Sokolov and Rintoul (2009)

215 formation in this region leads to greater mixing with deeper layers, replenishing surface nutrient concentrations and resulting
in higher export production (Marinov et al., 2006). Global P^* is $\sim 1.5\%$ higher in our glacfe experiments than in our lambfe
experiments resulting in a slightly larger CO_2 drawdown.

The sensitivity experiments provide additional information on the role of the Southern Ocean in our simulations. We find that
experiment lambfe10% is as efficient in drawing down CO_2 as the experiments where iron fluxes were only enhanced south of
220 30°S or 40°S (lambfe10%-30S, lambfe10%-40S) (Figure 4a,b)). This indicates that in our experiments iron fertilization in the
Southern Ocean south of 40°S is mainly responsible for the atmospheric CO_2 draw-down while fertilization elsewhere plays a
negligible role. On the other hand, a 14 ppm and 8.5 ppm CO_2 decrease is simulated in lambfe10%-50S and lambfe10%-60S,
respectively, compared to 15.3 ppm in lambfe10%.

Our experiments show that the ecosystem response north and south of $\sim 47^\circ\text{S}$ (which is roughly the modern SAF) are
225 of opposite sign (Table 3). While an increase in iron availability leads to an increase in NPP, diatom and coccolithophore

abundance, and consequently EP south of the SAF (Figure 5 and 6), the regions north of the SAF show a significant decline in all of these parameters. In our model, the EP increase occurs south of the SAF, where the surface nutrient concentrations are high (Figure A5a). Enhanced aeolian iron input leads to a more efficient use of nutrients in that region and results in a reduction in northward transport of nutrients north of the polar front (Figure A6) which in turn leads to a decrease in EP in the SAZ.

230 The relationship between atmospheric CO₂ and the iron flux south of 47°S follows (Figure 4b):

$$\Delta\text{CO}_2 = a(1 - b \times e^{-c \times (\text{SO}_{\text{fe}})^d}) \quad (5)$$

where ΔCO_2 is the atmospheric CO₂ anomaly in ppm compared to 70ka-control, SO_{fe} denotes the total iron input into the Southern Ocean south of 47°S in Gmolyr⁻¹, a= -21.51 ppm, b= 1.0, c= 0.487 (Gmolyr⁻¹)^{-d} and d= 0.66.

We also note that the CO₂ draw-down capacity levels out for high iron forcing. Both lambfe and glacfe masks with 20% iron solubility lead to a ~19 ppm CO₂ decrease. In our extreme experiment lambfe50%-47S, with an iron input south of 47°S almost 2.5 times higher than in lambfe20% and glacfe20%, only an additional 2 ppm CO₂ draw-down is simulated (Figure 4b). Our results therefore suggest that iron fertilization could have led to a maximum CO₂ decrease of ~19-21 ppm at 70 ka.

The enhanced iron flux leads to an increase in P_{reg} in the Southern Ocean, which is subsequently transported northward at depth by AABW. As a result, the globally averaged P*, and therefore the overall efficiency of the soft tissue pump, increases with Southern Ocean aeolian iron input (Figure 4c). As ocean circulation and ocean temperatures change only slightly in our experiments, the relationship between P* and the resulting CO₂ draw-down is almost linear (Figure A7) (Ito and Follows, 2005).

However, as the Southern Ocean iron flux increases, the overall iron fertilisation efficiency reduces. While export production increases south of 47°S, thus using nutrients more efficiently (Figure A8c) and reducing the nutrient advection north of the SAF (Figure A8b), nitrate limitation increases in the SAZ (Figure A9b,d and Figure A10a,b), leading to a decrease in export production. For example, in experiment lambfe20%, a 67% decrease in nitrate concentration is simulated between 40°S and 47°S (Figure A8b). At the same time, silicate limitation decreases in the SAZ (Figure A9e and Figure A10c) due to a southward shift of both coccolithophores and diatoms, and a decrease in diatoms between 40°S and 55°S (Figure A11). This further enhances silica availability in this region, consequently leading to a decrease in silicate limitation. Therefore, the total biological pump efficiency, represented here by changes in P* (Figure 4c) and Southern Ocean EP to NPP ratio (Figure A8a), saturate at high iron values due to nitrate limitation north of 50°S in the Southern Ocean. The global P* in lambfe20% and in lambfe50%-47S (Figure 4c) equal 0.63 and 0.65 respectively, suggesting a maximum efficiency of 65% in our experimental set-up.

The oceanic carbon reservoir in our sensitivity experiments increases between 20 and 130 GtC depending on the iron flux scenario (Figure 4d, blue shade). The simulated decrease in atmospheric CO₂, equivalent to 8-45 GtC (Figure 4d, red shade) leads to a decrease in surface air temperatures, as well as regional changes in precipitation and soil moisture. In addition, the lower atmospheric CO₂ concentration also reduces photosynthesis and consequently litter fall. The direct and indirect effects of a lower atmospheric CO₂ concentration result in a terrestrial carbon decrease of 16 to 88 GtC (Figure 4d, green shade), out of which 8 to 45 GtC decrease is from terrestrial vegetation while 8 to 43 GtC reduction is from soil carbon.

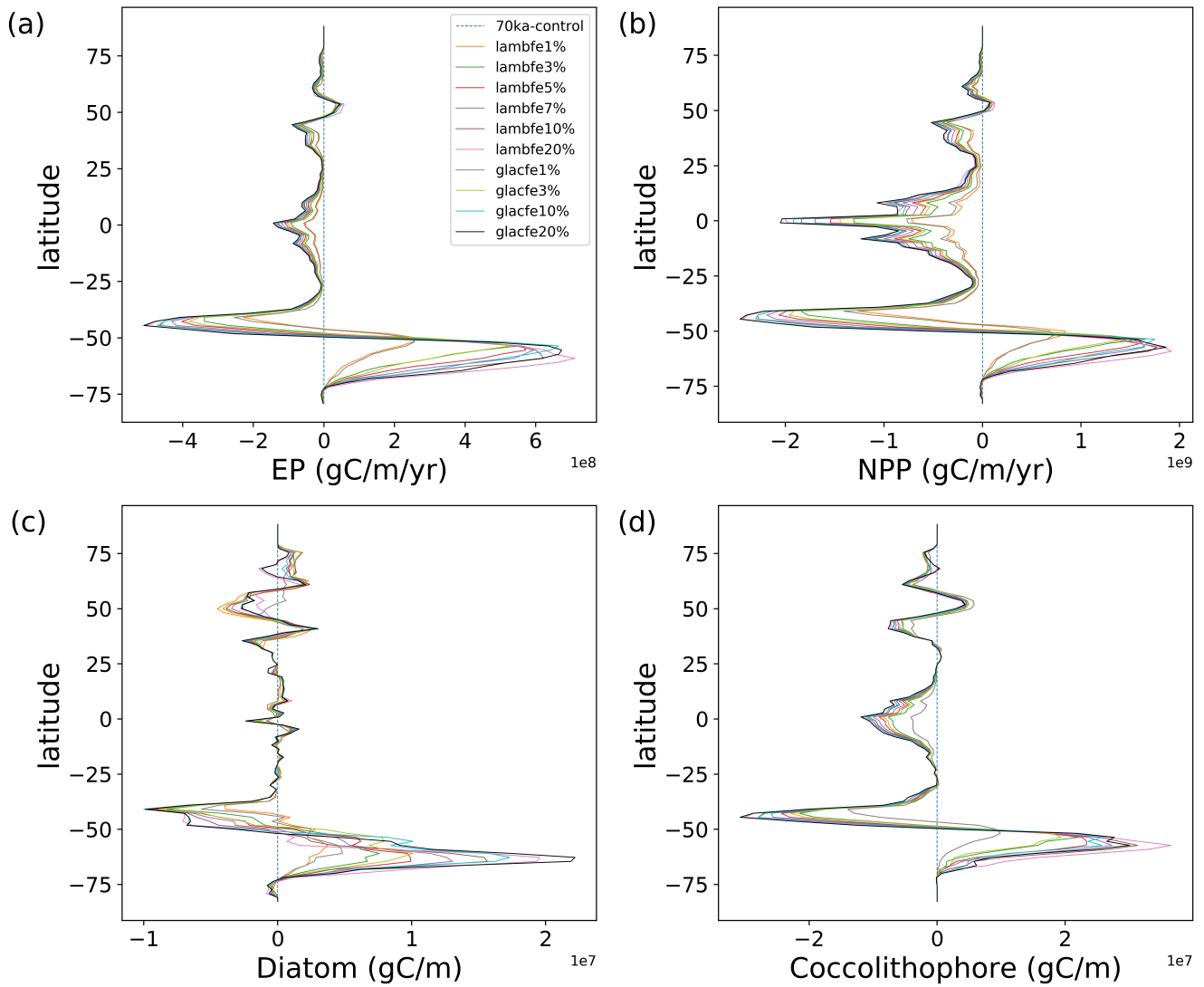


Figure 6. Zonally integrated anomalies of (a) EP ($\text{gC m}^{-1}\text{yr}^{-1}$) at 177.5m, (b) NPP ($\text{gC m}^{-1}\text{yr}^{-1}$), (c) Diatoms (gC m^{-1}) and (d) Coccolithophores (gC m^{-1}), compared to 70ka-control. Please note the multiplication factor allocated to each subpanel.

3.3 Impact of aeolian iron input on the distribution of oceanic carbon

260 As mentioned in the previous section, our sensitivity experiments do not show significant changes in the physical ocean conditions. However, enhanced iron input significantly impacts marine ecosystems. To understand the resulting ocean carbon changes, we start by describing changes in the simulated ecosystems for one of our sensitivity experiments, $\lambda_{\text{Fe}}3\%$, compared to 70ka-control. We choose $\lambda_{\text{Fe}}3\%$ (Figure A2) because earlier research shows that the λ_{Fe} Southern Ocean dust mask provides a better fit with available glacial dust flux proxy records than the λ_{Fe} mask (Saini et al., 2021). Furthermore, 265 a solubility factor of 3% corresponds to a likely estimate of iron solubility at 70 ka (see Methods) and has also been used in previously studies (Tagliabue et al., 2014; Lambert et al., 2015; Muglia et al., 2017; Yamamoto et al., 2019). All λ_{Fe} experiments with different solubility factors show similar anomaly patterns, only the magnitude of the changes varies as a function of solubility (Figure A11).

A ~ 9 ppm drop in atmospheric CO_2 is simulated in experiment $\lambda_{\text{Fe}}3\%$ with a global increase in EP by 1.3%, and a global 270 decrease in NPP by 6.7% (Table 3 and Table A1). Iron increase in the $\lambda_{\text{Fe}}3\%$ experiment leads to a 37% increase in diatoms and an 88% increase in coccolithophores in the AZ (Figure A4c,d). The simulated increased EP in the AZ (Figure 5a) leads to greater nutrient utilisation south of the APF (Figure A8c). On the contrary, because of lower nutrient availability, both diatoms and coccolithophores abundances decrease in the SAZ by 46% and 31% respectively (Figure A4c,d). Consequently, in the $\lambda_{\text{Fe}}3\%$ experiment, the EP increases by 98% in the AZ while it decreases by 17% in the SAZ compared to the 70ka-control 275 simulation (Figure 5a, 6a).

The overall Southern Ocean EP south of 30°S increases by $\sim 9\%$ in the $\lambda_{\text{Fe}}3\%$ experiment, the NPP changes become insignificant (Table 3), and the total biological pump efficiency increases by 6.7% (Table 3). In the North Pacific ($150^\circ\text{E};220^\circ\text{E};47^\circ\text{N};56^\circ\text{N}$), EP increases by 13%, while NPP increases by 7% due to a 82% increase in coccolithophores and 58% decrease in diatoms. Both NPP and EP decrease by $\sim 10\%$ in the North Atlantic ($60^\circ\text{W};0^\circ\text{E};47^\circ\text{N};56^\circ\text{N}$) where we 280 see an overall decrease in coccolithophores by 22% and an increase in diatoms by 16%.

The increased carbon export from the surface into the deep ocean increases DIC at all depths south of 47°S . The DIC rich bottom water is advected northward and leads to a stronger vertical DIC gradient in the ocean (Figure 7a and b). While DIC increases by 25 mmol m^{-3} in the deep Southern Ocean (south of 30°S , below 3000m), it does not increase uniformly across sectors: it increases by 22 mmol m^{-3} in the deep Indo-Pacific sector (below 3000m, Figure 7a), and by 29 mmol m^{-3} in the 285 deep Atlantic sector (below 3000m, Figure 7b). The positive DIC anomalies north of 30°S are associated with AABW and its northward spread into the Atlantic and the Indo-Pacific basins, therefore leading to a 10 mmol m^{-3} DIC increase in the deep Indo-Pacific and a 15 mmol m^{-3} increase in the deep Atlantic sector.

In contrast, lower DIC is simulated north of 47°S in the upper Pacific ocean (above 2000m), and within the North Atlantic Deep Water (NADW) and Antarctic Intermediate Water (AAIW) pathways in the Atlantic above 3000m. Simulated changes 290 in deep ocean oxygen concentrations (not shown) are opposite to the DIC changes indicating an increase in remineralised carbon in the deep ocean (Figure 8a,b). An increase in mixed layer alkalinity (Figure 7c and d) is simulated, partially due to the decrease in coccolithophores between 47°S - 50°N (Figure 6d and A4d). As a result of these changes in surface CaCO_3

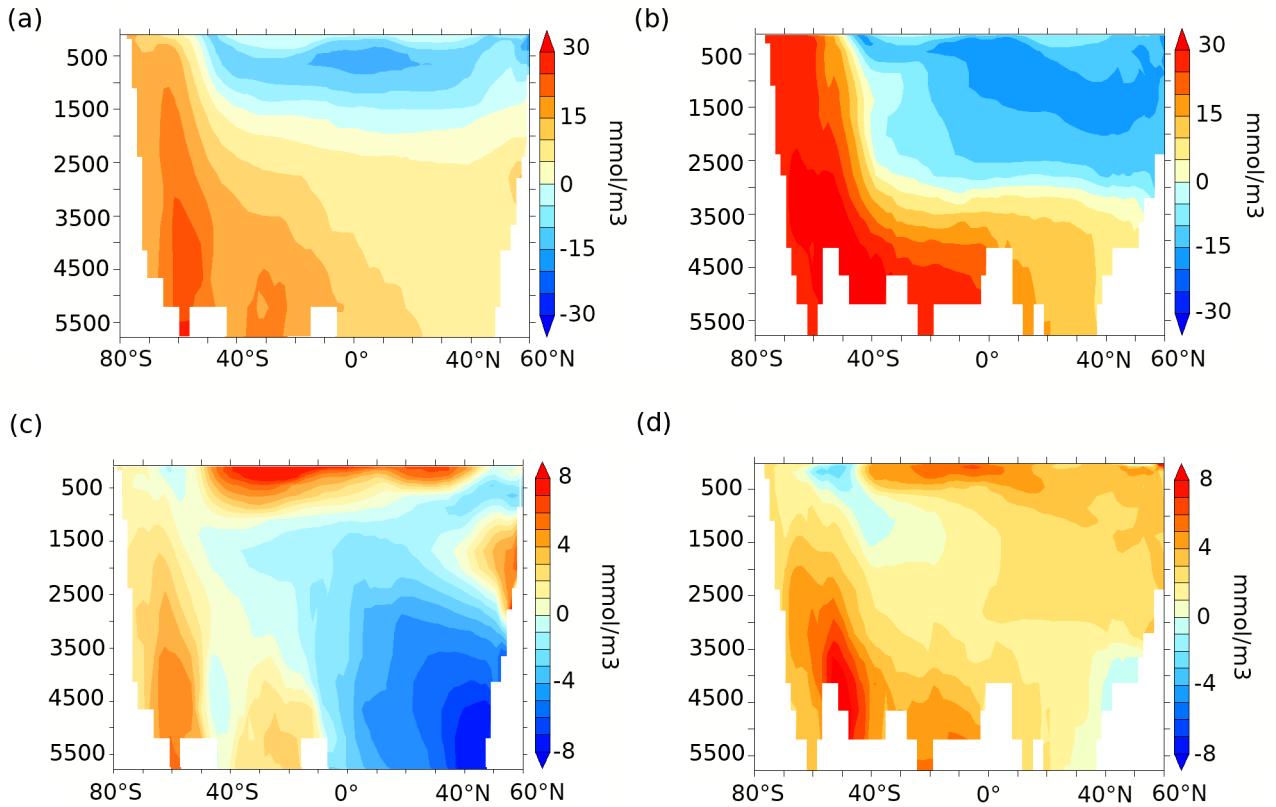


Figure 7. Zonally averaged DIC anomalies (mmol m^{-3}) over (a) the Indo-Pacific and (b) Atlantic, and zonally averaged alkalinity anomalies (mmol m^{-3}) over (c) the Indo-Pacific and (d) the Atlantic for $\lambda_{\text{Fe}}3\%$ compared to 70ka-control.

formation and subsequent changes in the subduction and sinking of CaCO_3 into deeper layers, reduced CaCO_3 dissolution at depth leads to lower alkalinity in the North Pacific, while higher CaCO_3 dissolution in the Southern Ocean and in the deep Atlantic leads to an alkalinity increase there (Figure 7c, d and Figure 8c, d).

To quantify the processes leading to changes in oceanic DIC, we decompose the changes in DIC into their remineralized, carbonate and preformed contributions (see Methods). In our 70ka-control simulation, the remineralization process leads to the generation of $131 \text{ mmol m}^{-3} C_{\text{reg}}$ in the deep ($\geq 3000\text{m}$ depth) Southern Ocean, which increases by 22.5 mmol m^{-3} in $\lambda_{\text{Fe}}3\%$ due to higher iron influx. Changes in the carbonate pump contribute marginally to the deep Southern Ocean DIC showing an increase of $3.16 \text{ mmol m}^{-3} C_{\text{CaCO}_3}$, whereas the preformed DIC contribution (C_{pref}) decreases by 0.66 mmol m^{-3} , compared to 70ka-control. North of 30°S , C_{reg} in $\lambda_{\text{Fe}}3\%$ increases by 14.7 mmol m^{-3} in the deep Indo-Pacific basin while both C_{CaCO_3} and C_{pref} decrease by 2 mmol m^{-3} and 2.6 mmol m^{-3} respectively (Figure 8a, c, e). The deep Atlantic

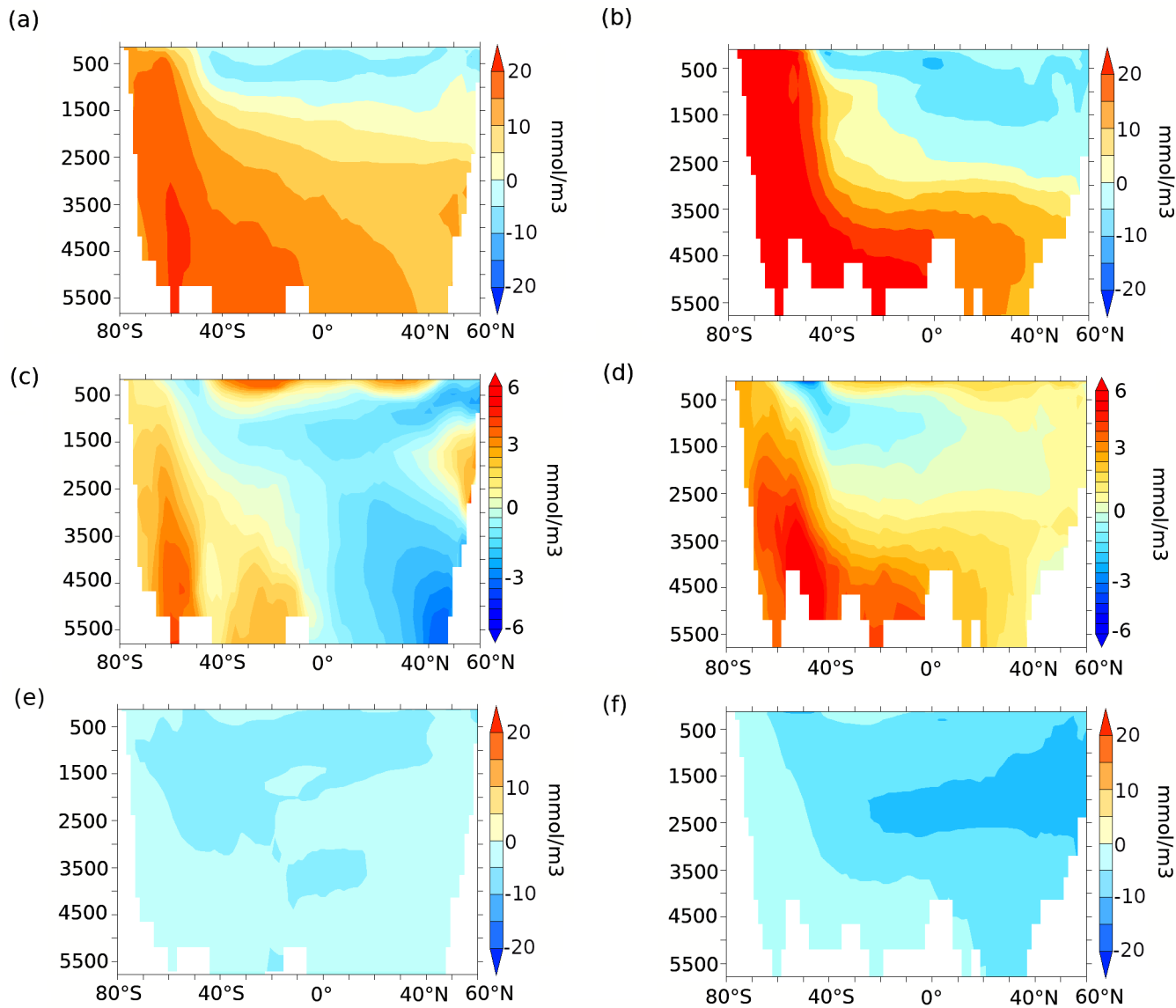


Figure 8. Zonally averaged (a, b) remineralized carbon (mmol m^{-3}), (c, d) carbon due to calcite dissolution (mmol m^{-3}) and (e, f) preformed carbon (mmol m^{-3}) anomalies for lambdafe3\% compared to 70ka-control in the Indo-Pacific (left panels) and the Atlantic (right panels). Please note that the color scale is different for subpanels c and d compared to other subpanels.

ocean shows an increase in C_{reg} by 16.3 mmol m^{-3} and in C_{CaCO_3} by 2 mmol m^{-3} in lambdafe3\% experiment, while C_{pref} decreases by 3.2 mmol m^{-3} (Figure 8b, d, f).

The colder climate at 70 ka BP leads to an overall decrease in NPP and EP compared to PI in our simulations (9.7% and 3%, respectively). The changes in NPP and EP are spatially heterogeneous and sensitive to changes in the length of the growing season, sea ice cover, and nutrient availability and are thus associated with shifts in plankton distribution. In the Southern Ocean, the $\sim 7.5\%$ reduction in NPP and 2% reduction in EP might be due to a shorter growing season for diatoms and coccolithophores (Saini et al., 2021), associated with a larger annual sea ice extent and lower SSTs at 70 ka BP. Both NPP and EP also decrease at low and mid latitudes.

Alkenone flux (Lamy et al., 2014; Martínez-García et al., 2014), as well as opal and organic carbon fluxes (Thöle et al., 2019; Amsler et al., 2022) reconstructed from subantarctic sediment cores suggest that EP was higher in the SAZ during MIS4 than present day. In addition, bottom water oxygenation records indicate a deep ocean oxygenation decrease during MIS4, which might suggest increased respired carbon storage in the deep ocean (Amsler et al., 2022) but could also reflect a change in ocean dynamics and water residence time. It has been suggested that the subantarctic EP increase during MIS4 was due to higher iron fluxes into the Southern Ocean. Higher dust deposition in the South Pacific and the South Atlantic at 70 ka is consistent with available paleo-proxy records (Martínez-García et al., 2011; Lambert et al., 2012; Lamy et al., 2014; Thöle et al., 2019). At the same time, palaeoceanographic records from the AZ suggest a decrease in EP during MIS4 (Anderson et al., 2009; Jaccard et al., 2013; Studer et al., 2015; Thöle et al., 2019; Amsler et al., 2022).

In our 70 ka simulations with enhanced iron input, EP increases in the AZ and polar frontal zone (between SAF and APF) and decreases in the SAZ, in contrast with most paleo-proxy records (Figure A5b). However, there is evidence that greater iron flux within the seasonal sea ice zone has led to higher diatom concentrations (Abelmann et al., 2006, 2015) and likely also EP in this region during glacial periods. In our study, as the iron input into the ocean increases, the nutrient utilisation increases in the AZ, consistent with the existing $\delta^{15}\text{N}$ records in the AZ at the MIS4/MIS5 transition (Studer et al., 2015; Ai et al., 2020). As a result, the nutrient advection into the SAZ is reduced, thus leading to an EP decrease in the SAZ. In addition, our simulated EP increase in the AZ during MIS4 compared to PI, and thus increase in regenerated carbon storage in the deep ocean, is consistent with some of the proxy records suggesting a decrease in deep ocean oxygenation in the AZ (Jaccard et al., 2016; Amsler et al., 2022). Our EP increase is also consistent with the increase in opal flux north of the APF (Amsler et al., 2022) at the MIS4 onset (Figure A5b). However, since proxy data for dust flux and EP is limited to only a few marine sites and ice cores, additional paleo-proxy records covering a larger area in the Southern Ocean during MIS4 are needed to better quantify the impact of iron fertilization during the glaciation.

Our results suggest that enhanced iron input south of the Antarctic polar front, i.e. south of $\sim 47^\circ\text{S}$ (Dong et al., 2006; Sokolov and Rintoul, 2009; Giglio and Johnson, 2016), is responsible for 100% of the simulated atmospheric CO_2 drawdown. This is in agreement with the hypothesis put forward by Marinov et al. (2006), which suggests that changes in the efficiency of the biological pump in the Antarctic zone play a dominant role in CO_2 drawdown. However, our results differ from Lambert et al. (2021), who find that $\sim 30\%$ of the simulated CO_2 decrease during the last glacial termination is due to enhanced aeolian iron input into the North Pacific in their simulations. While they use the same LGM dust flux, their iron input in the ocean

differs from our study. Lambert et al. (2021) assume 3.5 wt% iron fraction in the aeolian dust flux, whereas we use a global
340 map of percentage distribution of iron in dust (see Methods). More importantly, their solubility factor is not constant, but varies
non linearly with the magnitude of the dust flux.

While the two dust masks used here suggest an increase in aeolian iron deposition in the Atlantic sector of the Southern
Ocean during glacial times compared to PI, the iron input in glacfe is lower in the South Pacific compared to pife, whereas
lambfe is higher in the Pacific sector. Despite these differences in spatial patterns, the two iron masks (glacfe and lambfe)
345 with the same iron solubilities lead to similar decreases in atmospheric CO₂ in our simulations. This indicates that changes
in atmospheric CO₂ are more dependent on changes in solubility, than on regional differences in aeolian iron fluxes in the
Southern Ocean. The experiments using the glacfe mask are slightly more efficient in drawing down CO₂. One of the major
Antarctic Bottom Water formation sites is located in the Weddell Sea in our simulations, making the South Atlantic sector a
more efficient region for carbon sequestration. Higher iron dust input in the Weddell Sea in the glacfe experiments thus leads
350 to greater CO₂ drawdown compared to the lambfe experiments.

With no significant ocean circulation changes, changes in atmospheric CO₂ are a linear function of the overall efficiency
of the biological pump (P*, Figure A7). In agreement with earlier studies (Matsumoto et al., 2002; Tagliabue et al., 2014;
Lambert et al., 2015; Yamamoto et al., 2019), we find that the efficiency of the soft tissue pump increases south of 47°S, while
it decreases in the lower latitudes due to reduced northward advection of surface nutrients. The increase in the vertical nutrient
355 gradient leads to the eventual saturation of the ocean carbon uptake capacity.

We simulate a maximum of 16-18% increase in global P* in our experiments, leading to a maximum drop of 19 to 21 ppm
in CO₂. The timescale of this CO₂ draw-down in our idealised simulations, i.e. without transient changes in dust or transient
changes in ice sheet volume, is ~5000 years, which is consistent with the observed timescale of CO₂ transitions during MIS4
(Bereiter et al., 2015). If we define the plausible range of the large-scale average iron solubility in the ocean to be 1 to 10% at
360 70 ka BP, the corresponding range of atmospheric CO₂ draw-down is ~4 to 16 ppm. More likely, large-scale solubility in the
Southern Ocean at 70 ka ranged between 3 and 5%, which leads in our simulations to a CO₂ decline of 9 to 11 ppm (Figure 4b).

We find that the biological response to changes in iron fertilization not only depends on the iron solubility during glacial
periods but also on the iron solubility during warm periods. Our results are based on the assumption that the global average iron
solubility during warm periods equals ~1%. At higher initial values, the total potential draw-down of CO₂ would be smaller.
365 For example, for an assumed solubility during warm periods closer to ~3%, we simulate a range of CO₂ changes between 6.4
ppm (no change in solubility and glacial fluxes based on Lambert et al. (2015)) and 16.4 ppm (change to 20% solubility and
glacial fluxes based on Ohgaito et al. (2018)). This range reduces to 6.9 to 14.4 ppm if the initial solubility was 5% and to 6.7
to 6.9 ppm if the initial solubility was 20%.

Previous modeling studies obtained a 2 ppm drop in CO₂ using 2% iron solubility in the Southern Ocean under PI boundary
370 conditions (Tagliabue et al., 2014), while under LGM boundary conditions, using solubility factors between 1 and 2%, a 2-28
ppm drop in CO₂ was simulated by a hierarchy of models (Bopp et al., 2003; Tagliabue et al., 2009b; Lambert et al., 2015;
Muglia et al., 2017; Yamamoto et al., 2019). Using iron solubility factors of 3% and 10% under LGM conditions, Yamamoto
et al. (2019) simulated a 15.6 ppm to 20 ppm CO₂ reduction, while a solubility of 7% with varying dust masks led to a decrease

in CO₂ by 12-29 ppm in Lambert et al. (2021). A 12 ppm decrease at 70 ka was simulated in a transient simulation performed
375 with a model of intermediate complexity using 1% solubility (Menviel et al., 2012). Our results are consistent but in the lower
range of previous modelling estimates. Although our lowest estimate of a 4 ppm CO₂ reduction is in agreement with the studies
mentioned above, the upper limit of 16 ppm is lower than some previous estimates (e.g. Yamamoto et al. (2019), Lambert et al.
(2021)). This might be due to the comparatively larger simulated decrease in EP north of 47°S and in the equatorial Pacific in
our study compared to previous ones (Yamamoto et al., 2019).

380 None of the previous modelling studies on iron fertilisation simulate coccolithophores and diatoms' abundances prognos-
tically. By including four distinct classes of plankton in our model, we highlight the competitive dynamics between different
major phytoplankton functional types for light and nutrient availability. Coccolithophores contribute to the total carbon export
mainly in the polar frontal zone, while diatoms' contribution is in the Antarctic zone. As previously mentioned, carbon export
close to convection sites in the Southern Ocean can be more efficient in reducing atmospheric CO₂. Furthermore, while both
385 diatom and coccolithophores contribute to CO₂ uptake in the ocean through photosynthesis, coccolithophores produce CaCO₃
rich platelets, which reduce surface ocean alkalinity, thus reducing the CO₂ uptake efficiency. The inclusion of this competition
should be taken into account when investigating the impact of ecosystem changes on the global carbon cycle.

Our estimate of a 16 ppm CO₂ decrease with 10% iron solubility corresponds to half of the ~32 ppm CO₂ drop estimated
for the MIS4 transition (Bereiter et al., 2015). This suggests that enhanced aeolian iron input at the MIS4 transition could have
390 played a significant role in the CO₂ draw-down (Martínez-García et al., 2014; Kohfeld and Chase, 2017), but other processes
must also have contributed to the CO₂ decline. For example, an AMOC weakening (Piotrowski et al., 2005; Wilson et al.,
2015; O'Neill et al., 2021) could have enhanced ocean stratification, contributing 15-30 ppm to the CO₂ decrease during MIS4
(Thornalley et al., 2013; Yu et al., 2016; Menviel et al., 2017). An increase in ocean stratification at the MIS4 transition due to
changes in AABW properties (Adkins, 2013) could also have increased the deep ocean carbon content (Menviel et al., 2017),
395 thus contributing to the atmospheric CO₂ decline. Finally, both changes in oceanic circulation and a more efficient biological
pump could have enhanced sediment calcite dissolution, thus increasing ocean alkalinity and enhancing the CO₂ draw-down
(Boyle, 1988; Archer and Maier-Reimer, 1994; Yu et al., 2016; Kobayashi and Oka, 2018).

5 Conclusions

We use an Earth system model of intermediate complexity incorporating a newly developed ecosystem model to better constrain
400 the oceanic carbon uptake due to enhanced aeolian iron fluxes at the MIS4 transition. Based on a series of 70 ka sensitivity
experiments forced with two different aeolian iron flux masks and different iron solubility factors, we find that enhanced iron
input south of 47°S could have led to a 4 to 16 ppm CO₂ decline at 70 ka BP, with a most likely range of 9 to 11 ppm. Our
results suggest that the ocean's capacity to take up carbon decreases with increasing iron input because enhanced nutrient
utilisation in the Antarctic zone is compensated by decreased nutrient availability at mid and low latitudes. Enhanced aeolian
405 iron input at the MIS4 transition could thus explain up to 50% of the observed CO₂ drop at that time.

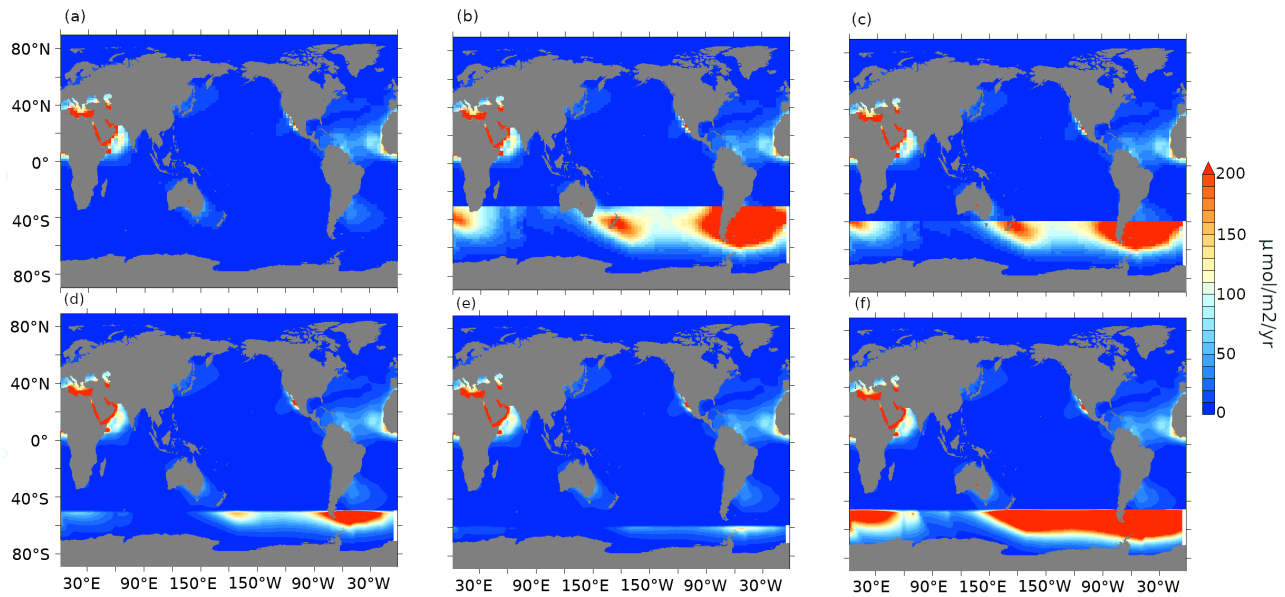


Figure A1. Aeolian iron dust flux ($\mu\text{mol m}^{-2} \text{yr}^{-1}$) for (a) pife1%, (b) lambfe10%-30S (iron flux equals lambfe10% south of 30°S and pife1% elsewhere), (c) lambfe10%-40S (same as lambfe10%-30S but for 40°S), (d) lambfe10%-50S, (e) lambfe10%-60S, (f) lambfe50%-47S (iron flux equals to lambfe50% south of 47°S and pife1% elsewhere).

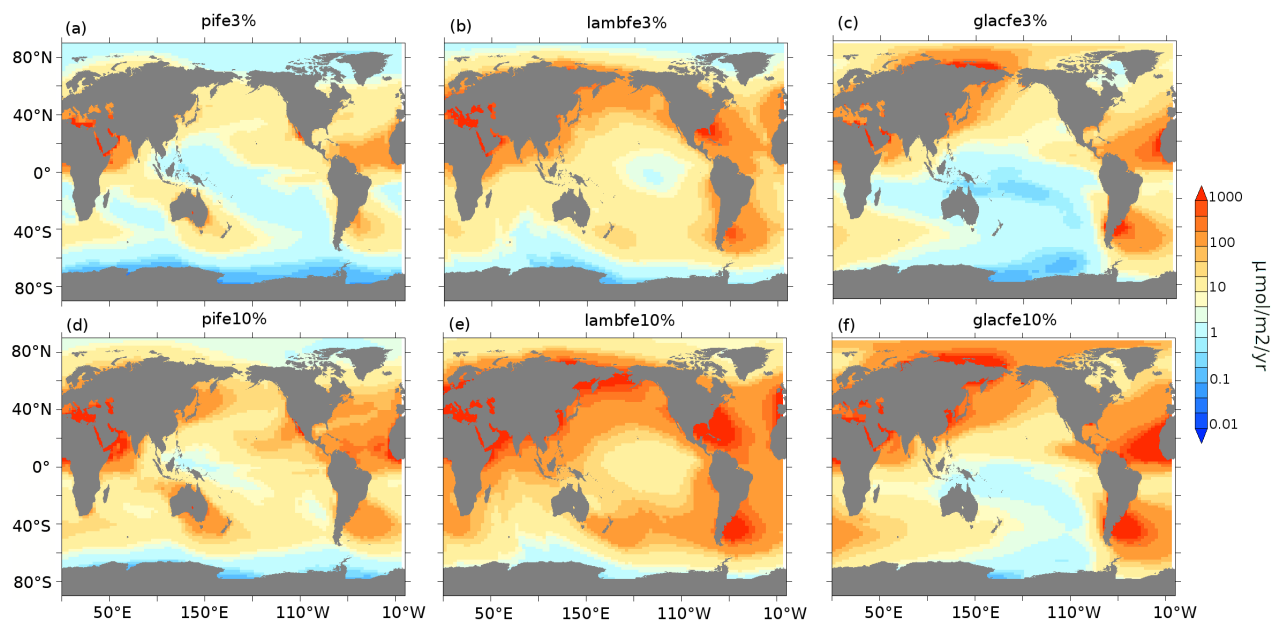


Figure A2. Aeolian iron dust fluxes ($\mu\text{mol m}^{-2} \text{yr}^{-1}$) for pife (a,d), lambfe (b,e) and glacfe (c,f) masks with 3% (top row) and 10% (bottom row) solubility factors.

Table A1. Globally integrated NPP and EP values. Percentage changes from 70ka-control experiment are provided in brackets.

Experiment	Global NPP (Pg C _{yr} ⁻¹)	Global Export Production at 177.5m depth (Pg C _{yr} ⁻¹)
PI-control (pife1%)	47.45	7.19
70ka-control (pife1%)	42.81	6.98
lambfe1%	41.40 (-3.2%)	7.02 (+0.6%)
lambfe3%	39.93 (-6.7%)	7.07 (+1.3%)
lambfe5%	39.44 (-7.8%)	7.11 (+1.9%)
lambfe7%	38.78 (-9.4%)	7.09 (+1.6%)
lambfe10%	38.49 (-10%)	7.12 (+2%)
lambfe20%	37.97 (-11%)	7.16 (+2.6%)
glacfe1%	41.06 (-4%)	7.00 (+0.3%)
glacfe3%	39.32 (-8.1%)	7.03 (+0.7%)
glacfe10%	38.09 (-11%)	7.07 (+1.3%)
glacfe20%	37.67 (-12%)	7.06 (+1%)

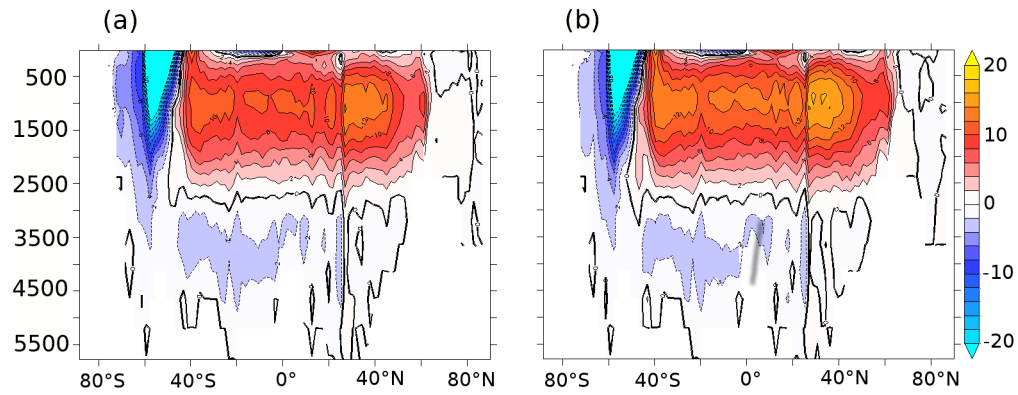


Figure A3. Atlantic meridional streamfunction (Sv) at (a) 70 ka BP and (b) PI

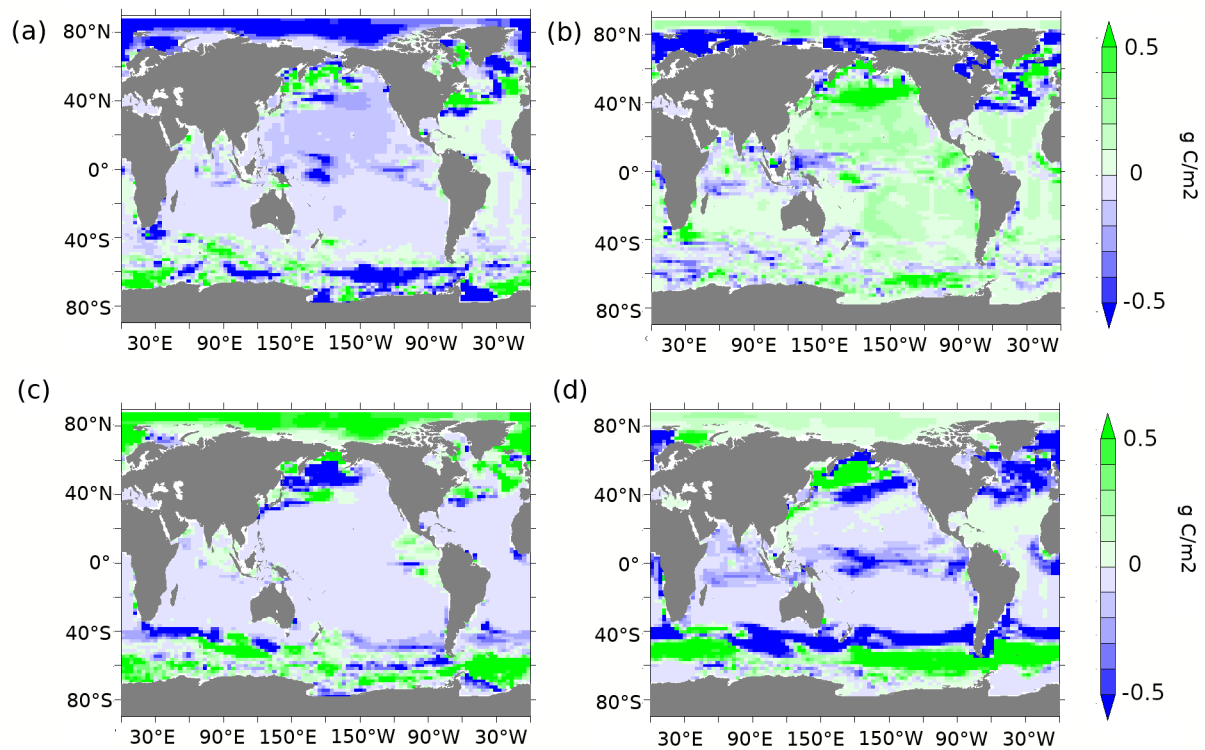


Figure A4. (a) Diatoms and (b) coccolithophores abundance anomalies (gC m^{-2}) at 70 ka compared to PI. (c) Diatoms and (d) coccolithophores abundance anomalies (gC m^{-2}) in $\lambda_{f3}\%$ compared to 70ka-control.

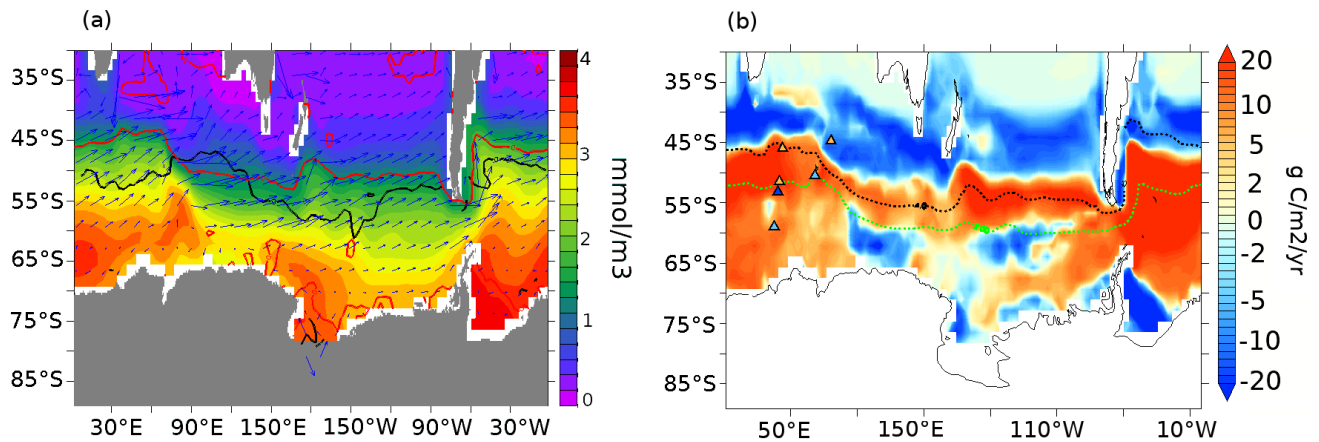


Figure A5. (a) Surface nitrate concentrations (mmol m^{-3}) for the 70ka-control experiment. The overlaid contours show the zero isoline of annual wind stress curl (black) and the zero contour of EP anomalies (red) between lambfe3% and 70ka-control (pife1%). Blue arrows represent surface currents; (b) Export production anomalies ($\text{gC m}^{-2} \text{yr}^{-1}$) at 177.5m depth for lambfe3% compared to PI-control (pife1%) with opal flux (triangles) proxy records from (Amsler et al., 2022) (left of 50°E) and from (Thöle et al., 2019) (right of 50°E) to show qualitative comparison between model and data. Dark (light) orange represents significantly higher (slightly higher) and dark (light) blue represents significantly lower (slightly lower) values at 70ka compared to PI. Overlaid dashed contours represent modern SAF in black and APF in green based on the definition of Sokolov and Rintoul (2009).

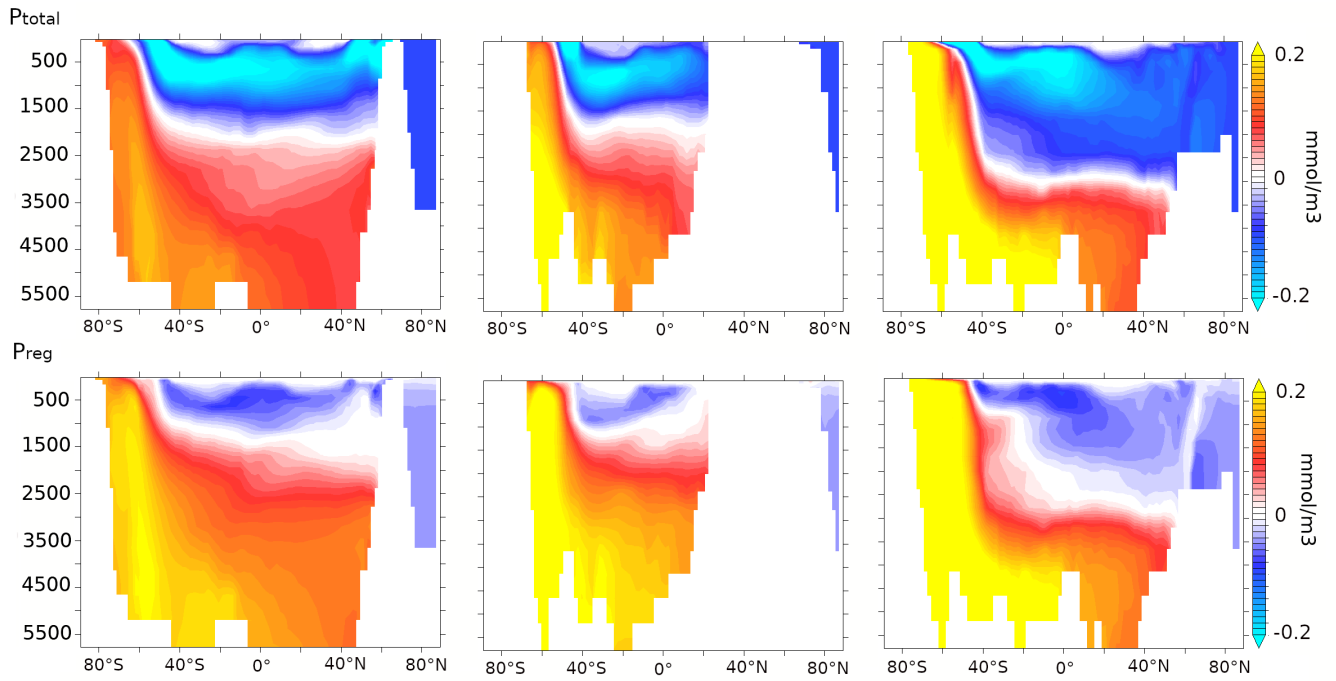


Figure A6. $\lambda_{\text{P}} 3\%$ to 70ka-control ($\lambda_{\text{P}} 1\%$) anomalies of zonally averaged (top panels) total phosphate and (bottom panels) regenerated phosphate concentration anomalies (mmol m^{-3}) over (left) the Pacific, (center) Indian and (right) Atlantic basins.

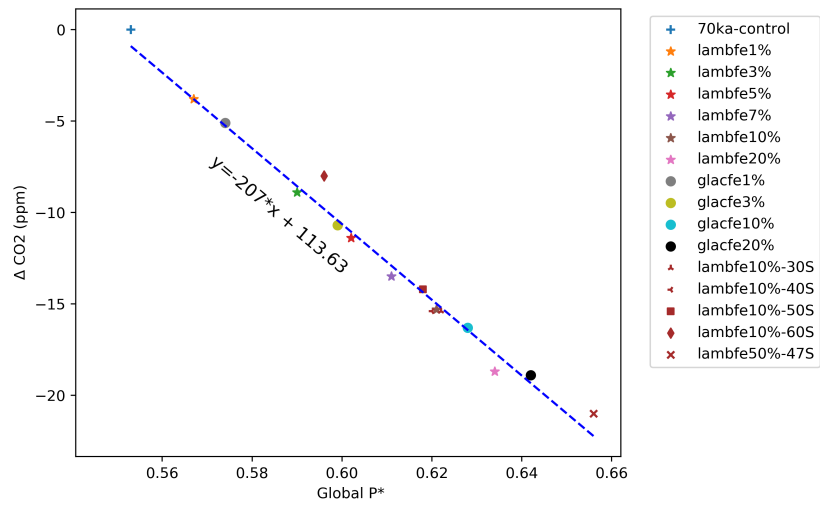


Figure A7. Atmospheric CO₂ (ppm) anomalies as a function of global P*. Slope= -207 ppm (compared to -312 ppm as per (Ito and Follows, 2005)).

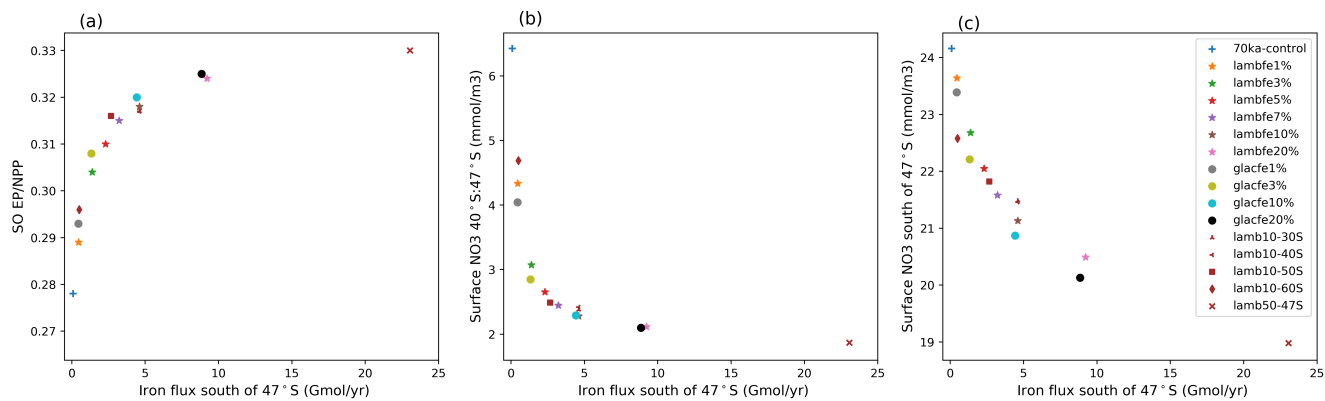


Figure A8. (a) Ratio of EP to NPP averaged over the Southern Ocean (south of 30°S), (b) surface nitrate concentration averaged over 40°S:47°S (mmol m^{-3}), and (c) surface nitrate concentration south of 47°S (mmol m^{-3}) as a function of the aeolian iron flux (Gmol yr^{-1}) into the Southern Ocean south of 47°S.

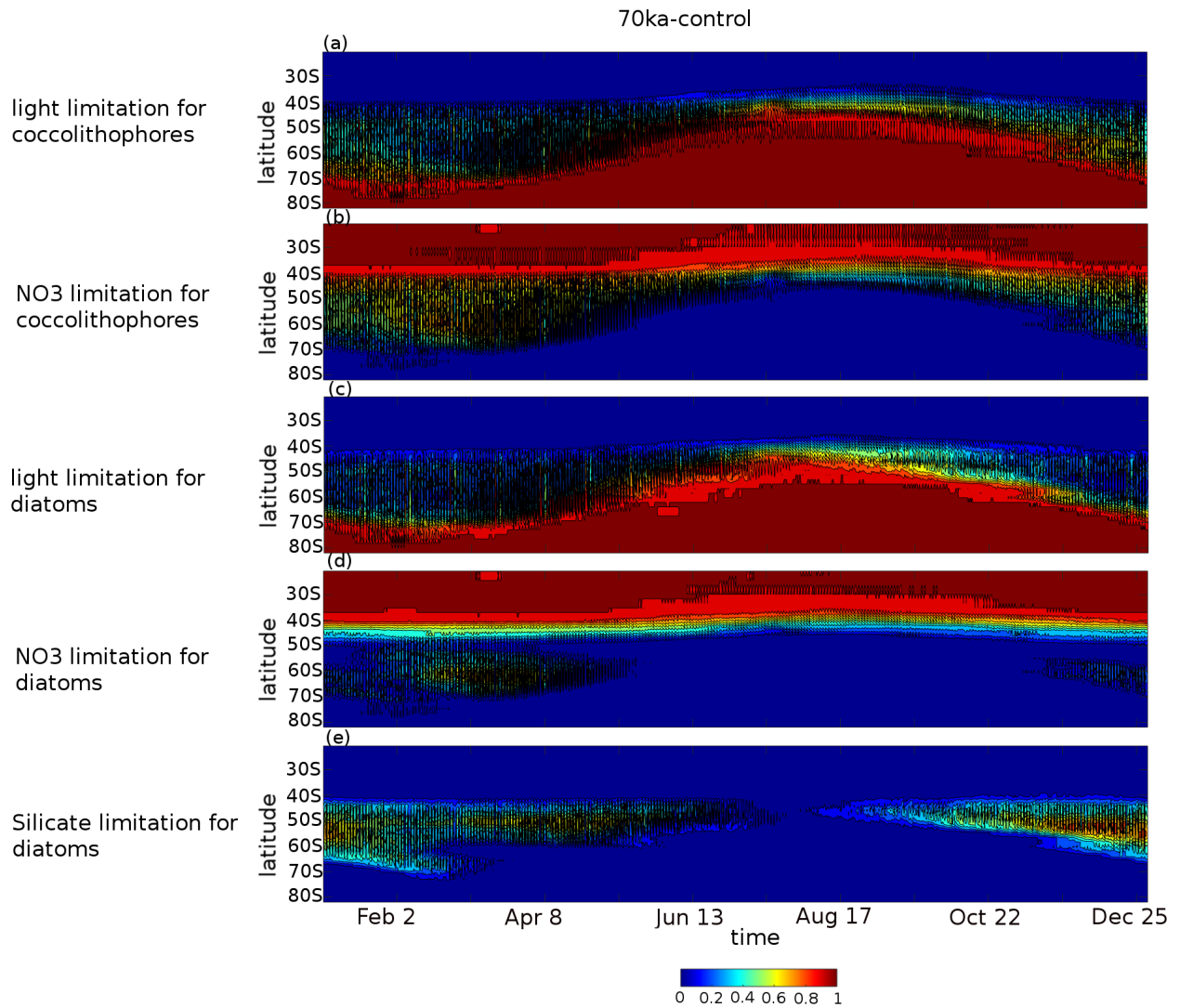


Figure A9. Hovmöller diagrams of the proportion of ocean grid cells per latitude band for the 70ka-control experiment for which (a) light is limiting coccolithophore growth (b) nitrate is limiting coccolithophore growth, (c) light is limiting diatom growth (d) nitrate is limiting diatom growth, (e) silicate is limiting diatom growth. In all the subpanels, if shade=1, then all ocean grid cells at that latitude band are limited by the respective limiting factor, if shade=0.5, then half of them are.

lambfe20%- 70ka-control

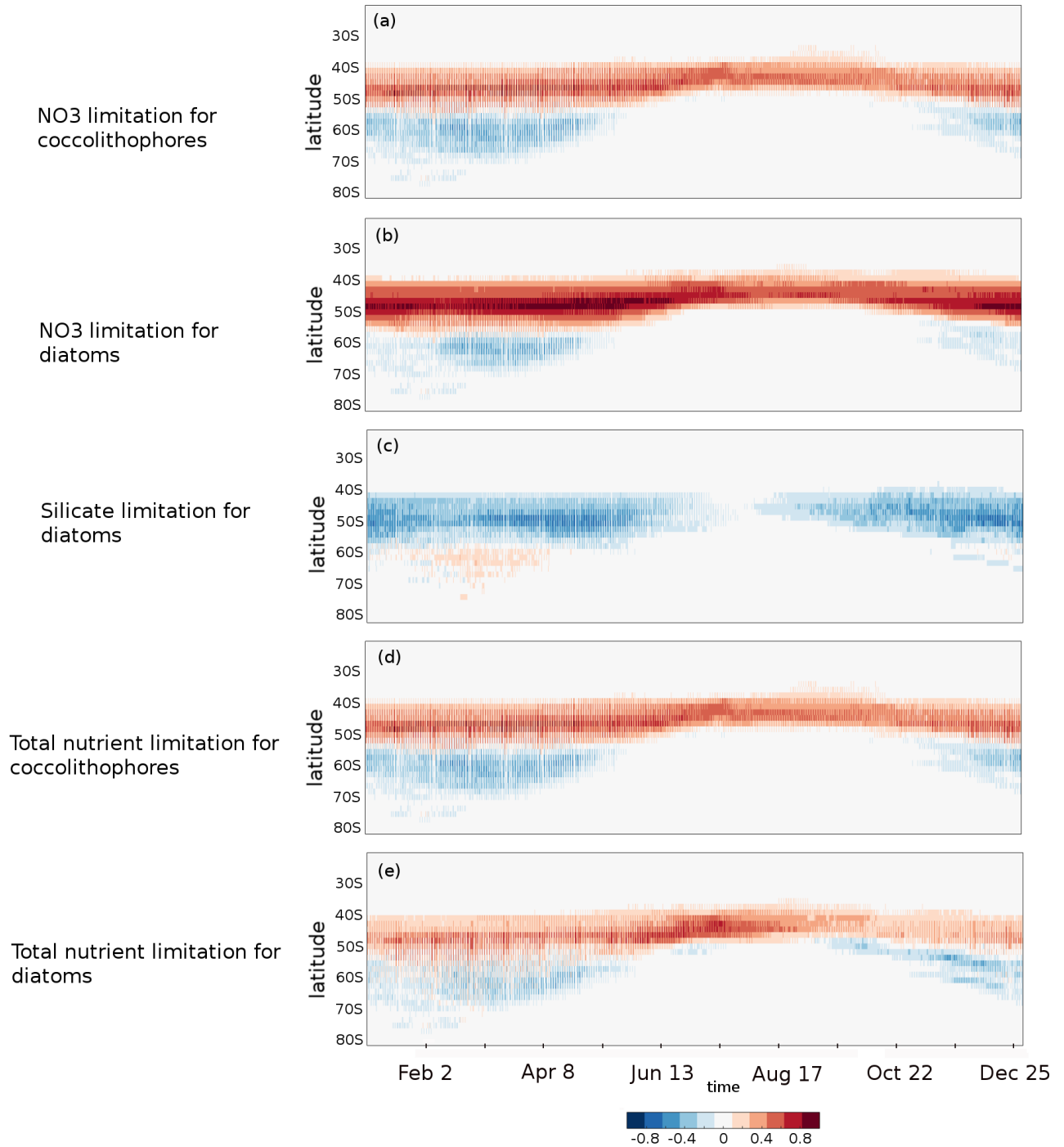


Figure A10. Hovmöller diagrams of the lambfe20% minus 70ka-control anomaly in the proportion of ocean grid cells per latitude band for which (a) nitrate is limiting coccolithophore growth, (b) nitrate is limiting diatom growth, (c) silicate is limiting diatom growth, (d) either of the macronutrients is limiting coccolithophore growth and (e) either of the macronutrients is limiting diatom growth.

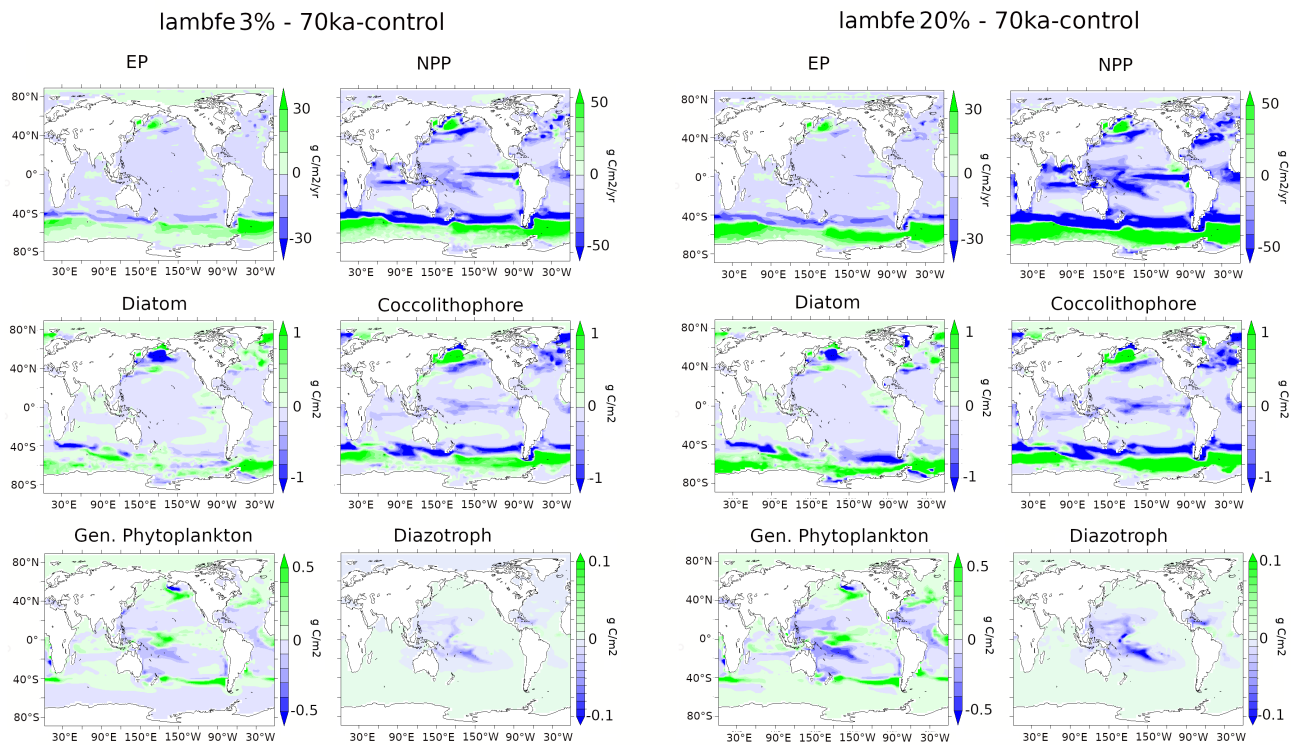


Figure A11. Ecosystem anomalies between lambfe3%-70ka-control and lambfe20%-70ka-control including EP ($\text{gC m}^{-2}\text{yr}^{-1}$) at 177.5m, NPP ($\text{gC m}^{-2}\text{yr}^{-1}$), diatoms (gC m^{-2}), coccolithophores (gC m^{-2}), general phytoplanktons (gC m^{-2}), and diazotrophs (gC m^{-2}).

Data availability. All the final data from modelling simulations is published on UNSW ResData repository (<https://doi.org/10.26190/unsworks/24072>)

Author contributions. HS performed all the simulations and analyses. KJM and LM supervised the research and assisted in the interpretation of the results. HS, LM and KJM drafted the manuscript. KK provided scientific support for the KMBM3 model and comments on an advanced draft of the manuscript.

410 *Competing interests.* The authors declare that they have no conflict of interest.

Acknowledgements. Himadri Saini acknowledges funding from the University International Postgraduate Award scheme (UNSW). KJM and LM acknowledge support from the Australian Research Council (DP180100048, DP180102357, SR200100008 and FT180100606). KK is supported by the Global Change Through Time Programme administered by the New Zealand Ministry of Business, Innovation and Employment. All experiments were performed on the computational facility of NCI owned by the Australian National University through
415 awards under the Merit Allocation Scheme and the UNSW HPC at NCI Scheme.

References

- Abe-Ouchi, A., Saito, F., Kawamura, K., Raymo, M. E., Okuno, J., Takahashi, K., and Blatter, H.: Insolation-driven 100,000-year glacial cycles and hysteresis of ice-sheet volume, *Nature*, 500, 190–193, 2013.
- Abelmann, A., Gersonde, R., Cortese, G., Kuhn, G., and Smetacek, V.: Extensive phytoplankton blooms in the Atlantic sector of the glacial
420 Southern Ocean, *Paleoceanography*, 21, 2006.
- Abelmann, A., Gersonde, R., Knorr, G., Zhang, X., Chaplignin, B., Maier, E., Esper, O., Friedrichsen, H., Lohmann, G., Meyer, H., et al.: The seasonal sea-ice zone in the glacial Southern Ocean as a carbon sink, *Nature communications*, 6, 1–13, 2015.
- Adkins, J. F.: The role of deep ocean circulation in setting glacial climates, *Paleoceanography*, 28, 539–561, 2013.
- Ahn, J. and Brook, E. J.: Atmospheric CO₂ and climate on millennial time scales during the last glacial period, *Science*, 322, 83–85, 2008.
- 425 Ai, X. E., Studer, A. S., Sigman, D. M., Martínez-García, A., Fripiat, F., Thöle, L. M., Michel, E., Gottschalk, J., Arnold, L., Moretti, S., et al.: Southern Ocean upwelling, Earth’s obliquity, and glacial-interglacial atmospheric CO₂ change, *Science*, 370, 1348–1352, 2020.
- Amsler, H. E., Thöle, L. M., Stimac, I., Geibert, W., Ikehara, M., Kuhn, G., Esper, O., and Jaccard, S. L.: Bottom water oxygenation changes in the Southwestern Indian Ocean as an indicator for enhanced respired carbon storage since the last glacial inception, *Climate of the Past*, 18, 1797–1813, 2022.
- 430 Anderson, R., Ali, S., Bradtmiller, L., Nielsen, S., Fleisher, M., Anderson, B., and Burckle, L.: Wind-driven upwelling in the Southern Ocean and the deglacial rise in atmospheric CO₂, *science*, 323, 1443–1448, 2009.
- Anderson, R. F., Barker, S., Fleisher, M., Gersonde, R., Goldstein, S. L., Kuhn, G., Mortyn, P. G., Pahnke, K., and Sachs, J. P.: Biological response to millennial variability of dust and nutrient supply in the Subantarctic South Atlantic Ocean, *Philosophical Transactions of the Royal Society A: Mathematical, Physical and Engineering Sciences*, 372, 20130054, 2014.
- 435 Archer, D. and Maier-Reimer, E.: Effect of deep-sea sedimentary calcite preservation on atmospheric CO₂ concentration, *Nature*, 367, 260–263, 1994.
- Aumont, O. and Bopp, L.: Globalizing results from ocean in situ iron fertilization studies, *Global Biogeochemical Cycles*, 20, 2006.
- Aumont, O., Maier-Reimer, E., Blain, S., and Monfray, P.: An ecosystem model of the global ocean including Fe, Si, P colimitations, *Global Biogeochemical Cycles*, 17, 2003.
- 440 Baker, A., Jickells, T., Witt, M., and Linge, K.: Trends in the solubility of iron, aluminium, manganese and phosphorus in aerosol collected over the Atlantic Ocean, *Marine Chemistry*, 98, 43–58, 2006.
- Bassinot, F. C., Labeyrie, L. D., Vincent, E., Quidelleur, X., Shackleton, N. J., and Lancelot, Y.: The astronomical theory of climate and the age of the Brunhes-Matuyama magnetic reversal, *Earth and Planetary Science Letters*, 126, 91–108, 1994.
- Batchelor, C. L., Margold, M., Krapp, M., Murton, D. K., Dalton, A. S., Gibbard, P. L., Stokes, C. R., Murton, J. B., and Manica, A.: The
445 configuration of Northern Hemisphere ice sheets through the Quaternary, *Nature Communications*, 10, 1–10, 2019.
- Bereiter, B., Lüthi, D., Siegrist, M., Schüpbach, S., Stocker, T. F., and Fischer, H.: Mode change of millennial CO₂ variability during the last glacial cycle associated with a bipolar marine carbon seesaw, *Proceedings of the National Academy of Sciences*, 109, 9755–9760, 2012.
- Bereiter, B., Eggleston, S., Schmitt, J., Nehrbass-Ahles, C., Stocker, T. F., Fischer, H., Kipfstuhl, S., and Chappellaz, J.: Revision of the EPICA Dome C CO₂ record from 800 to 600 kyr before present, *Geophysical Research Letters*, 42, 542–549, 2015.
- 450 Berger, A.: Long-term variations of daily insolation and Quaternary climatic changes, *Journal of Atmospheric Sciences*, 35, 2362–2367, 1978.

- Bopp, L., Kohfeld, K. E., Le Quéré, C., and Aumont, O.: Dust impact on marine biota and atmospheric CO₂ during glacial periods, *Paleoceanography*, 18, 2003.
- Boyle, E. A.: The role of vertical chemical fractionation in controlling late Quaternary atmospheric carbon dioxide, *Journal of Geophysical Research: Oceans*, 93, 15 701–15 714, 1988.
- 455 Brovkin, V., Ganopolski, A., Archer, D., and Munhoven, G.: Glacial CO₂ cycle as a succession of key physical and biogeochemical processes, *Climate of the Past*, 8, 251–264, 2012.
- Conway, T. M., Wolff, E. W., Röthlisberger, R., Mulvaney, R., and Elderfield, H.: Constraints on soluble aerosol iron flux to the Southern Ocean at the Last Glacial Maximum, *Nature Communications*, 6, 1–9, 2015.
- 460 De Deckker, P., Arnold, L. J., van der Kaars, S., Bayon, G., Stuut, J.-B. W., Perner, K., dos Santos, R. L., Uemura, R., and Demuro, M.: Marine Isotope Stage 4 in Australasia: a full glacial culminating 65,000 years ago—global connections and implications for human dispersal, *Quaternary Science Reviews*, 204, 187–207, 2019.
- Dong, S., Sprintall, J., and Gille, S. T.: Location of the Antarctic polar front from AMSR-E satellite sea surface temperature measurements, *Journal of Physical Oceanography*, 36, 2075–2089, 2006.
- 465 Eby, M., Zickfeld, K., Montenegro, A., Archer, D., Meissner, K., and Weaver, A. J.: Lifetime of anthropogenic climate change: Millennial time scales of potential CO₂ and surface temperature perturbations, *Journal of Climate*, 22, 2501–2511, <https://doi.org/10.1175/2008JCLI2554.1>, 2009.
- Eggleston, S., Schmitt, J., Bereiter, B., Schneider, R., and Fischer, H.: Evolution of the stable carbon isotope composition of atmospheric CO₂ over the last glacial cycle, *Paleoceanography*, 31, 434–452, 2016.
- 470 EPICA Community Members, Augustin, L., Barbante, C., Barnes, P. R., Barnola, J. M., Bigler, M., Castellano, E., Cattani, O., Chappellaz, J., Dahl-Jensen, D., Delmonte, B., et al.: Eight glacial cycles from an Antarctic ice core, *Nature*, 429, 623–628, 2004.
- Fanning, A. F. and Weaver, A. J.: An atmospheric energy-moisture balance model: Climatology, interpentadal climate change, and coupling to an ocean general circulation model, *Journal of Geophysical Research: Atmospheres*, 101, 15 111–15 128, <https://doi.org/10.1029/96JD01017>, 1996.
- 475 Ferrari, R., Jansen, M. F., Adkins, J. F., Burke, A., Stewart, A. L., and Thompson, A. F.: Antarctic sea ice control on ocean circulation in present and glacial climates, *Proceedings of the National Academy of Sciences*, 111, 8753–8758, 2014.
- Francois, R., Altabet, M. A., Yu, E.-F., Sigman, D. M., Bacon, M. P., Frank, M., Bohrmann, G., Bareille, G., and Labeyrie, L. D.: Contribution of Southern Ocean surface-water stratification to low atmospheric CO₂ concentrations during the last glacial period, *Nature*, 389, 929–935, 1997.
- 480 Gebhardt, H., Sarnthein, M., Grootes, P. M., Kiefer, T., Kuehn, H., Schmieder, F., and Röhl, U.: Paleonutrient and productivity records from the subarctic North Pacific for Pleistocene glacial terminations I to V, *Paleoceanography*, 23, 2008.
- Giglio, D. and Johnson, G. C.: Subantarctic and polar fronts of the Antarctic Circumpolar Current and Southern Ocean heat and freshwater content variability: A view from Argo, *Journal of Physical Oceanography*, 46, 749–768, 2016.
- Grant, K., Rohling, E., Bar-Matthews, M., Ayalon, A., Medina-Elizalde, M., Ramsey, C. B., Satow, C., and Roberts, A.: Rapid coupling
485 between ice volume and polar temperature over the past 150,000 years, *Nature*, 491, 744–747, 2012.
- Heinze, C., Maier-Reimer, E., and Winn, K.: Glacial pCO₂ reduction by the world ocean: Experiments with the Hamburg carbon cycle model, *Paleoceanography*, 6, 395–430, 1991.
- Hibler, W. D.: A dynamic thermodynamic sea ice model, *Journal of physical oceanography*, 9, 815–846, 1979.

- Hunke, E. C. and Dukowicz, J. K.: An elastic–viscous–plastic model for sea ice dynamics, *Journal of Physical Oceanography*, 27, 1849–1867, 1997.
- 490 Ito, A., Myriokefalitakis, S., Kanakidou, M., Mahowald, N. M., Scanza, R. A., Hamilton, D. S., Baker, A. R., Jickells, T., Sarin, M., Bikkina, S., et al.: Pyrogenic iron: The missing link to high iron solubility in aerosols, *Science advances*, 5, eaau7671, 2019.
- Ito, T. and Follows, M. J.: Preformed phosphate, soft tissue pump and atmospheric CO₂, *Journal of Marine Research*, 63, 813–839, 2005.
- Jaccard, S. L., Haug, G. H., Sigman, D. M., Pedersen, T. F., Thierstein, H. R., and Rohl, U.: Glacial/interglacial changes in subarctic North Pacific stratification, *Science*, 308, 1003–1006, 2005.
- 495 Jaccard, S. L., Hayes, C. T., Martinez-Garcia, A., Hodell, D. A., Anderson, R. F., Sigman, D. M., and Haug, G.: Two modes of change in Southern Ocean productivity over the past million years, *Science*, 339, 1419–1423, 2013.
- Jaccard, S. L., Galbraith, E. D., Martínez-García, A., and Anderson, R. F.: Covariation of deep Southern Ocean oxygenation and atmospheric CO₂ through the last ice age, *Nature*, 530, 207–210, 2016.
- 500 Jouzel, J., Masson-Delmotte, V., Cattani, O., Dreyfus, G., Falourd, S., Hoffmann, G., Minster, B., Nouet, J., Barnola, J.-M., Chappellaz, J., et al.: Orbital and millennial Antarctic climate variability over the past 800,000 years, *Science*, 317, 793–796, 2007.
- Kalnay, E., Kanamitsu, M., Kistler, R., Collins, W., Deaven, D., Gandin, L., Iredell, M., Saha, S., White, G., Woollen, J., et al.: The NCEP/NCAR 40-year reanalysis project, *Bulletin of the American meteorological Society*, 77, 437–472, 1996.
- Keller, D. P., Oschlies, A., and Eby, M.: A new marine ecosystem model for the University of Victoria earth system climate model, *Geoscientific Model Development*, 5, 1195–1220, <https://doi.org/10.5194/gmd-5-1195-2012>, 2012.
- 505 Khatiwala, S., Schmittner, A., and Muglia, J.: Air-sea disequilibrium enhances ocean carbon storage during glacial periods, *Science advances*, 5, eaaw4981, 2019.
- Kleman, J., Fastook, J., Ebert, K., Nilsson, J., and Caballero, R.: Pre-LGM Northern Hemisphere ice sheet topography, *Climate of the Past*, 9, 2365–2378, 2013.
- 510 Kobayashi, H. and Oka, A.: Response of atmospheric pCO₂ to glacial Changes in the Southern Ocean amplified by carbonate compensation, *Paleoceanography and Paleoclimatology*, 33, 1206–1229, 2018.
- Kohfeld, K. E. and Chase, Z.: Temporal evolution of mechanisms controlling ocean carbon uptake during the last glacial cycle, *Earth and Planetary Science Letters*, 472, 206–215, 2017.
- Kohfeld, K. E. and Harrison, S. P.: DIRTMAP: the geological record of dust, *Earth-Science Reviews*, 54, 81–114, 2001.
- 515 Kohfeld, K. E., Le Quéré, C., Harrison, S. P., and Anderson, R. F.: Role of marine biology in glacial-interglacial CO₂ cycles, *Science*, 308, 74–78, 2005.
- Kohfeld, K. E., Graham, R., De Boer, A., Sime, L., Wolff, E., Le Quéré, C., and Bopp, L.: Southern Hemisphere westerly wind changes during the Last Glacial Maximum: paleo-data synthesis, *Quaternary Science Reviews*, 68, 76–95, 2013.
- Kucera, M., Weinelt, M., Kiefer, T., Pflaumann, U., Hayes, A., Weinelt, M., Chen, M.-T., Mix, A. C., Barrows, T. T., Cortijo, E., et al.: Reconstruction of sea-surface temperatures from assemblages of planktonic foraminifera: multi-technique approach based on geographically constrained calibration data sets and its application to glacial Atlantic and Pacific Oceans, *Quaternary Science Reviews*, 24, 951–998, 2005.
- 520 Kvale, K., Keller, D. P., Koeve, W., Meissner, K. J., Somes, C. J., Yao, W., and Oschlies, A.: Explicit silicate cycling in the Kiel Marine Biogeochemistry Model version 3 (KMBM3) embedded in the UVic ESCM version 2.9, *Geoscientific Model Development*, 14, 7255–7285, 2021.
- 525

- Kvale, K. F., Meissner, K., Keller, D., Eby, M., and Schmittner, A.: Explicit planktic calcifiers in the university of victoria earth system climate model, version 2.9, *Atmosphere-Ocean*, 53, 332–350, 2015a.
- Kvale, K. F., Meissner, K., and Keller, D.: Potential increasing dominance of heterotrophy in the global ocean, *Environmental Research Letters*, 10, 074 009, 2015b.
- 530 Lambeck, K., Purcell, A., Zhao, J., and SVENSSON, N.-O.: The Scandinavian ice sheet: from MIS 4 to the end of the last glacial maximum, *Boreas*, 39, 410–435, 2010.
- Lambert, F., Delmonte, B., Petit, J.-R., Bigler, M., Kaufmann, P. R., Hutterli, M. A., Stocker, T. F., Ruth, U., Steffensen, J. P., and Maggi, V.: Dust-climate couplings over the past 800,000 years from the EPICA Dome C ice core, *Nature*, 452, 616–619, 2008.
- Lambert, F., Bigler, M., Steffensen, J. P., Hutterli, M., and Fischer, H.: Centennial mineral dust variability in high-resolution ice core data
535 from Dome C, Antarctica, *Climate of the Past*, 8, 609–623, 2012.
- Lambert, F., Tagliabue, A., Shaffer, G., Lamy, F., Winckler, G., Farias, L., Gallardo, L., and De Pol-Holz, R.: Dust fluxes and iron fertilization in Holocene and Last Glacial Maximum climates, *Geophysical Research Letters*, 42, 6014–6023, 2015.
- Lambert, F., Opazo, N., Ridgwell, A., Winckler, G., Lamy, F., Shaffer, G., Kohfeld, K., Ohgaito, R., Albani, S., and Abe-Ouchi, A.: Regional
540 patterns and temporal evolution of ocean iron fertilization and CO₂ drawdown during the last glacial termination, *Earth and Planetary Science Letters*, 554, 116 675, 2021.
- Lamy, F., Gersonde, R., Winckler, G., Esper, O., Jaeschke, A., Kuhn, G., Ullermann, J., Martínez-García, A., Lambert, F., and Kilian, R.: Increased dust deposition in the Pacific Southern Ocean during glacial periods, *Science*, 343, 403–407, 2014.
- Lüthi, D., Le Floch, M., Bereiter, B., Blunier, T., Barnola, J.-M., Siegenthaler, U., Raynaud, D., Jouzel, J., Fischer, H., Kawamura, K., et al.: High-resolution carbon dioxide concentration record 650,000–800,000 years before present, *Nature*, 453, 379–382, 2008.
- 545 Maher, B., Prospero, J., Mackie, D., Gaiero, D., Hesse, P., and Balkanski, Y.: Global connections between aeolian dust, climate and ocean biogeochemistry at the present day and at the last glacial maximum, *Earth-Science Reviews*, 99, 61–97, 2010.
- Mahowald, N. M., Muhs, D. R., Levis, S., Rasch, P. J., Yoshioka, M., Zender, C. S., and Luo, C.: Change in atmospheric mineral aerosols in response to climate: Last glacial period, preindustrial, modern, and doubled carbon dioxide climates, *Journal of Geophysical Research Atmospheres*, 111, <https://doi.org/10.1029/2005JD006653>, 2006.
- 550 Marinov, I., Gnanadesikan, A., Toggweiler, J., and Sarmiento, J. L.: The southern ocean biogeochemical divide, *Nature*, 441, 964–967, 2006.
- Martin, J. H.: Iron Hypothesis of CO₂ Change, *Paleoceanography*, 5, 1–13, 1990.
- Martínez-García, A., Rosell-Melé, A., Jaccard, S. L., Geibert, W., Sigman, D. M., and Haug, G. H.: Southern Ocean dust–climate coupling over the past four million years, *Nature*, 476, 312–315, 2011.
- Martínez-García, A., Sigman, D. M., Ren, H., Anderson, R. F., Straub, M., Hodell, D. A., Jaccard, S. L., Eglinton, T. I., and Haug, G. H.:
555 Iron fertilization of the Subantarctic Ocean during the last ice age, *Science*, 343, 1347–1350, 2014.
- Matsumoto, K., Sarmiento, J. L., and Brzezinski, M. A.: Silicic acid leakage from the Southern Ocean: A possible explanation for glacial atmospheric pCO₂, *Global Biogeochemical Cycles*, 16, 5–1–5–23, <https://doi.org/10.1029/2001gb001442>, 2002.
- Meissner, K., Weaver, A. J., Matthews, H. D., and Cox, P. M.: The role of land surface dynamics in glacial inception: A study with the UVic Earth System Model, *Climate Dynamics*, 21, 515–537, <https://doi.org/10.1007/s00382-003-0352-2>, 2003.
- 560 Meissner, K., McNeil, B. I., Eby, M., and Wiebe, E. C.: The importance of the terrestrial weathering feedback for multimillennial coral reef habitat recovery, *Global Biogeochemical Cycles*, 26, 1–20, <https://doi.org/10.1029/2011GB004098>, 2012.

- Mengis, N., Keller, D., MacDougall, A., Eby, M., Wright, N., Meissner, K., Oschlies, A., Schmittner, A., Matthews, H. D., and Zickfeld, K.: Evaluation of the University of Victoria Earth System Climate Model version 2.10 (UVic ESCM 2.10), Geoscientific Model Development, in press, 2020.
- 565 Menking, J. A., Shackleton, S. A., Bauska, T. K., Buffen, A. M., Brook, E. J., Barker, S., Severinghaus, J. P., Dyonisius, M. N., and Petrenko, V. V.: Multiple carbon cycle mechanisms associated with the glaciation of Marine Isotope Stage 4, *Nature communications*, 13, 1–10, 2022.
- Menviel, L., Joos, F., and Ritz, S.: Simulating atmospheric CO₂, 13C and the marine carbon cycle during the Last Glacial–Interglacial cycle: possible role for a deepening of the mean remineralization depth and an increase in the oceanic nutrient inventory, *Quaternary Science*
- 570 *Reviews*, 56, 46–68, 2012.
- Menviel, L., Mouchet, A., Meissner, K. J., Joos, F., and England, M. H.: Impact of oceanic circulation changes on atmospheric δ13CO₂, *Global Biogeochemical Cycles*, 29, 1944–1961, 2015.
- Menviel, L., Yu, J., Joos, F., Mouchet, A., Meissner, K., and England, M. H.: Poorly ventilated deep ocean at the Last Glacial Maximum inferred from carbon isotopes: A data-model comparison study, *Paleoceanography*, 32, 2–17, 2017.
- 575 Muglia, J., Somes, C. J., Nickelsen, L., and Schmittner, A.: Combined effects of atmospheric and seafloor iron fluxes to the glacial ocean, *Paleoceanography*, 32, 1204–1218, <https://doi.org/10.1002/2016PA003077>, 2017.
- Nickelsen, L., Keller, D. P., and Oschlies, A.: A dynamic marine iron cycle module coupled to the University of Victoria Earth System Model: The Kiel Marine Biogeochemical Model 2 for UVic 2.9, *Geoscientific Model Development*, 8, 1357–1381, <https://doi.org/10.5194/gmd-8-1357-2015>, 2015.
- 580 Ohgaito, R., Abe-Ouchi, A., O’Ishi, R., Takemura, T., Ito, A., Hajima, T., Watanabe, S., and Kawamiya, M.: Effect of high dust amount on surface temperature during the Last Glacial Maximum: A modelling study using MIROC-ESM, *Climate of the Past*, 14, 1565–1581, <https://doi.org/10.5194/cp-14-1565-2018>, 2018.
- Oka, A., Abe-Ouchi, A., Chikamoto, M. O., and Ide, T.: Mechanisms controlling export production at the LGM: Effects of changes in oceanic physical fields and atmospheric dust deposition, *Global Biogeochemical Cycles*, 25, 2011.
- 585 O’Neill, C. M., Hogg, A. M., Ellwood, M. J., Opdyke, B. N., and Eggins, S. M.: Sequential changes in ocean circulation and biological export productivity during the last glacial–interglacial cycle: A model–data study, *Climate of the Past*, 17, 171–201, 2021.
- Pacanowski, R.: MOM2 documentation user’s guide and reference manual: GFDL ocean group technical report, Geophysical Fluid Dynamics Laboratory (GFDL), National Oceanic and Atmospheric Administration, Princeton, NJ, 1995.
- Petit, J.-R., Jouzel, J., Raynaud, D., Barkov, N. I., Barnola, J.-M., Basile, I., Bender, M., Chappellaz, J., Davis, M., Delaygue, G., et al.:
- 590 *Climate and atmospheric history of the past 420,000 years from the Vostok ice core, Antarctica*, *Nature*, 399, 429, 1999.
- Piotrowski, A. M., Goldstein, S. L., Hemming, S. R., and Fairbanks, R. G.: Temporal relationships of carbon cycling and ocean circulation at glacial boundaries, *Science*, 307, 1933–1938, 2005.
- Saini, H., Kvale, K., Chase, Z., Kohfeld, K. E., Meissner, K. J., and Menviel, L.: Southern Ocean ecosystem response to Last Glacial Maximum boundary conditions, *Paleoceanography and Paleoclimatology*, p. e2020PA004075, 2021.
- 595 Schmittner, A., Oschlies, A., Giraud, X., Eby, M., and Simmons, H. L.: A global model of the marine ecosystem for long-term simulations: Sensitivity to ocean mixing, buoyancy forcing, particle sinking, and dissolved organic matter cycling, *Global Biogeochemical Cycles*, 19, 1–17, <https://doi.org/10.1029/2004GB002283>, 2005.
- Schroth, A. W., Crusius, J., Sholkovitz, E. R., and Bostick, B. C.: Iron solubility driven by speciation in dust sources to the ocean, *Nature Geoscience*, 2, 337–340, 2009.

- 600 Semtner Jr, A. J.: A model for the thermodynamic growth of sea ice in numerical investigations of climate, *Journal of Physical Oceanography*, 6, 379–389, 1976.
- Shoenfelt, E. M., Sun, J., Winckler, G., Kaplan, M. R., Borunda, A. L., Farrell, K. R., Moreno, P. I., Gaiero, D. M., Recasens, C., Sambrotto, R. N., et al.: High particulate iron (II) content in glacially sourced dusts enhances productivity of a model diatom, *Science advances*, 3, e1700314, 2017.
- 605 Shoenfelt, E. M., Winckler, G., Lamy, F., Anderson, R. F., and Bostick, B. C.: Highly bioavailable dust-borne iron delivered to the Southern Ocean during glacial periods, *Proceedings of the National Academy of Sciences*, 115, 11180–11185, 2018.
- Sigman, D. M. and Boyle, E. A.: Glacial/interglacial variations in atmospheric carbon dioxide, *Nature*, 407, 859–869, 2000.
- Sigman, D. M., Hain, M. P., and Haug, G. H.: The polar ocean and glacial cycles in atmospheric CO₂ concentration, *Nature*, 466, 47–55, 2010.
- 610 Sokolov, S. and Rintoul, S. R.: Circumpolar structure and distribution of the Antarctic Circumpolar Current fronts: 1. Mean circumpolar paths, *Journal of Geophysical Research: Oceans*, 114, 2009.
- Stephens, B. B. and Keeling, R. F.: The influence of Antarctic sea ice on glacial–interglacial CO₂ variations, *Nature*, 404, 171–174, 2000.
- Studer, A. S., Sigman, D. M., Martínez-García, A., Benz, V., Winckler, G., Kuhn, G., Esper, O., Lamy, F., Jaccard, S. L., Wacker, L., et al.: Antarctic Zone nutrient conditions during the last two glacial cycles, *Paleoceanography*, 30, 845–862, 2015.
- 615 Tagliabue, A., Bopp, L., and Aumont, O.: Evaluating the importance of atmospheric and sedimentary iron sources to Southern Ocean biogeochemistry, *Geophysical Research Letters*, 36, 2009a.
- Tagliabue, A., Bopp, L., Roche, D. M., Bouttes, N., Dutay, J.-C., Alkama, R., Kageyama, M., Michel, E., and Paillard, D.: Quantifying the roles of ocean circulation and biogeochemistry in governing ocean carbon-13 and atmospheric carbon dioxide at the last glacial maximum, *Climate of the Past*, 5, 695–706, 2009b.
- 620 Tagliabue, A., Aumont, O., and Bopp, L.: The impact of different external sources of iron on the global carbon cycle, *Geophysical Research Letters*, 41, 920–926, 2014.
- Thöle, L. M., Amsler, H. E., Moretti, S., Auderset, A., Gilgannon, J., Lippold, J., Vogel, H., Crosta, X., Mazaud, A., Michel, E., et al.: Glacial-interglacial dust and export production records from the Southern Indian Ocean, *Earth and planetary science letters*, 525, 115–116, 2019.
- 625 Thornalley, D. J., Barker, S., Becker, J., Hall, I. R., and Knorr, G.: Abrupt changes in deep Atlantic circulation during the transition to full glacial conditions, *Paleoceanography*, 28, 253–262, 2013.
- Toggweiler, J.: Origin of the 100,000-year timescale in Antarctic temperatures and atmospheric CO₂, *Paleoceanography*, 23, 2008.
- Waelbroeck, C., Labeyrie, L., Michel, E., Duplessy, J. C., McManus, J., Lambeck, K., Balbon, E., and Labracherie, M.: Sea-level and deep water temperature changes derived from benthic foraminifera isotopic records, *Quaternary Science Reviews*, 21, 295–305, 2002.
- 630 Watson, A. J., Vallis, G. K., and Nikurashin, M.: Southern Ocean buoyancy forcing of ocean ventilation and glacial atmospheric CO₂, *Nature Geoscience*, 8, 861–864, 2015.
- Weaver, A. J., Eby, M., Wiebe, E. C., Bitz, C. M., Duffy, P. B., Ewen, T. L., Fanning, A. F., Holland, M. M., MacFadyen, A., Matthews, H. D., Meissner, K., Saenko, O., Schmittner, A., Wang, H., and Yoshimori, M.: The UVic earth system climate model: Model description, climatology, and applications to past, present and future climates, *Atmosphere-Ocean*, 39, 361–428, <https://doi.org/10.1080/07055900.2001.9649686>, 2001.
- 635 Williams, R. G. and Follows, M. J.: *Ocean dynamics and the carbon cycle: Principles and mechanisms*, Cambridge University Press, 2011.

- Wilson, D. J., Piotrowski, A. M., Galy, A., and Banakar, V. K.: Interhemispheric controls on deep ocean circulation and carbon chemistry during the last two glacial cycles, *Paleoceanography*, 30, 621–641, 2015.
- 640 Wolff, E., Barbante, C., Becagli, S., Bigler, M., Boutron, C., Castellano, E., De Angelis, M., Federer, U., Fischer, H., Fundel, F., et al.: Changes in environment over the last 800,000 years from chemical analysis of the EPICA Dome C ice core, *Quaternary Science Reviews*, 29, 285–295, 2010.
- Wolff, E. W., Fischer, H., Fundel, F., Ruth, U., Twarloh, B., Littot, G. C., Mulvaney, R., Röthlisberger, R., de Angelis, M., Boutron, C. F., et al.: Southern Ocean sea-ice extent, productivity and iron flux over the past eight glacial cycles, *Nature*, 440, 491–496, 2006.
- 645 Yamamoto, A., Abe-Ouchi, A., Ohgaito, R., Ito, A., and Oka, A.: Glacial CO₂ decrease and deep-water deoxygenation by iron fertilization from glaciogenic dust, *Climate of the Past Discussions*, pp. 1–31, <https://doi.org/10.5194/cp-2019-31>, 2019.
- Yu, J., Menviel, L., Jin, Z., Thornalley, D., Barker, S., Marino, G., Rohling, E., Cai, Y., Zhang, F., Wang, X., et al.: Sequestration of carbon in the deep Atlantic during the last glaciation, *Nature Geoscience*, 9, 319–324, 2016.
- 650 Zhang, Y., Mahowald, N., Scanza, R. A., Journet, E., Desboeufs, K., Albani, S., Kok, J. F., Zhuang, G., Chen, Y., Cohen, D. D., Paytan, A., Patey, M. D., Achterberg, E. P., Engelbrecht, J. P., and Fomba, K. W.: Modeling the global emission, transport and deposition of trace elements associated with mineral dust, *Biogeosciences*, 12, 5771–5792, <https://doi.org/10.5194/bg-12-5771-2015>, 2015.